Inspection of copper canisters for spent nuclear fuel by means of ultrasound

Ultrasonic imaging of EB weld, theory of harmonic imaging of welds, NDE of cast iron

Tadeusz Stepinski, Fredrik Lingvall, Ping Wu

Uppsala University, Signals and Systems,

Department of Materials Science, Sweden

July 2001

SKB

Inspection of copper canisters for spent nuclear fuel by means of ultrasound

Ultrasonic imaging of EB weld, theory of harmonic imaging of welds, NDE of cast iron

Tadeusz Stepinski, Fredrik Lingvall, Ping Wu

Uppsala University, Signals and Systems,

Department of Materials Science, Sweden

July 2001

Summary

The objective of task presented in the first chapter, *ultrasonic imaging of EB weld* is to investigate imaging methods capable of improving ultrasonic imaging of defects in EB-welds. Algorithms based on ideas from ultrasonic tomography were examined as the first step. After a concise review of literature in the field of tomography the attention is focused on *synthetic focusing* and particularly on using linear phased array systems for imaging. Synthetic focusing is a technique where the focusing is performed by software after gathering the ultrasonic data. General principles of *synthetic aperture focusing technique* (SAFT) - a synthetic focusing technique especially suitable for linear ultrasonic arrays are presented. Problems related to the application of SAFT to ultrasonic transducers with large apertures are identified and the solution is proposed. It appears that when the probe becomes larger (i.e., cannot be regarded as a point source) the ultrasonic pulses that it generates will be smeared by its spatial impulse response (SIR). This impairs the spatial resolution achieved for the finite aperture probes comparing to the point source. Thus, a proper application of synthetic focusing requires taking into account the spatially varying probe's SIR. The SIR has to be calculated (measured) in the interesting points of space and than deconvolved. A technique for deconvolving the SIR based on Wiener filter is proposed and illustrated by experimental results. Some preliminary results from immersion testing of copper blocks using the ALLIN system in our lab facility are presented.

Nonlinear propagation of plane waves in fluids based on the Burgers equation is investigated in the second chapter. The presented method is basically adopted from the existing literature although some modification has been made to adapt to our situation. The solution has been re-derived and two alternative forms feasible for computer calculation are given and some numerical results are presented. The calculated results show how the harmonics evolve as the plane wave propagates. It should be noted that the work presented here is at its preliminary stage, the goal of the present and future work is to build a simulating tool for material harmonic imaging technology.

The theory of *phase conjugation* is presented and different methods of wave phase conjugation (WPC) are reviewed and characterized in the third chapter. The ability of WPC to self-adaptive focus ultrasonic waves in inhomogeneous media makes it interesting in the application to the inspection of as EB welds. The WPC can be performed either in time or frequency domain. Time domain method, known as time reversal mirrors is reviewed in some detail with focus on its applications to NDT. Frequency domain techniques use nonlinear piezoelectric or magnetic materials. The choice of magneto-acoustic phase conjugation, performed in nonlinear magnetic ceramics as a candidate for the feasibility demonstration is motivated. Details of the preliminary experiment with high frequency NDE application (10 MHz) are presented.

NDE methods suitable for the *characterization of cast iron* are reviewed in the fourth chapter. Two groups of methods that could be used in an industrial environment, those based on ultrasound and on eddy current measurement are presented in some detail. The review is focused on sensing the interaction of elastic waves with the microstructure of cast iron. It is explained how three different features of ultrasound, the sound velocity, the attenuation and the backscattering, can be used for the characterization.

Sammanfattning

Målet med uppgiften presenterad i första kapitlet, *ultrasonic imaging of EB weld*, är att undersöka metoder för att förbättra bildpresentationen av defekter i EB-svetsar. Algoritmer som är baserade på idéer från ultraljudstomografi undersöktes i det första steget. Efter en litteraturundersökning inom ultrljudstomografi koncentrerades sedan arbetet på syntetisk fokusering speciellt riktat mot linjära arrayer. Syntetisk fokuserning är en teknik där fokuserning sker med programvara efter att ultraljudsdata är insamlat. Principerna för SAFT (*eng. synthetic aperture focusing techninque*), vilket är en teknik speciellt lämpade för linjära arrayer, presenteras först. Sedan diskuteras problem som uppkommer med sökare som har an stor apertur och en lösning på problemet föreslås. Det visar sig att när sökaren blir större (dvs. när sökaren ej kan ses som en punktkälla) kommer ultrljudspulserna att smetas ut beroende på det spatiella impulssvaret hos sökaren (eng. spatial impulse response - SIR). Detta försämrar den spatiella upplösningen när sökare med ändlig apertur används jämfört med punktkällor. Detta betyder att hänsyn måste tagas till den spatialt varierande SIR som sökaren har för att syntetisk fokusering skall fungera tillfredställande. Dvs. det spatiella impulsssvaret måste beräknas (mätas) i de punkter som är av intresse för att sedan avfaltas. En metod för avfaltning av sökarens SIR baserad på Wienerfiltrering föreslås och illustreras med experimentella resultat. Några preliminära resultat från imersionsproving av kopparblock med vårat ALLIN-system visas.

Ickelinjär utbredning av plana vågor i vätskor baserad på Burgers ekvation har undersökts i kapitel två. Den metod som används är i princip hämtad från litteraturen med några modifieringar för att passa till våran mätsituation. Lösning härleds samt två metoder lämpliga för datorimplementering presenteras med numeriska resultat. De numerska resultaten visar hur de harmoniska komponenterna utvecklas när den planavågen utbreder sig. Notera dock att arbetet är preliminärt och målet med framtida undersökningar är att utveckla ett simuleringsverktyg för material-harmoniska komponenter.

I kapitel tre presenteras teorin om fas-konjugering och olika metoder för WPC (*eng. wave phase conjugation*) granskas och karakteriseras. Möjligheten att med WPC konstruera självfokuserande system i ickehomogena material gör metoden intressant för inspektion av EB-svetsar. Detta kan utföras både i tids- och frekvensdomänen. Metoden som i tidsdomänen är känd som TRM (*eng. time reversal mirror*) granskas med fokus på NDT tillämpningar. Frekvensdomän metoderna använder ickelinjära piezoelektriska eller magnetiska material. Valet av en magneto-akustisk metod med ickelinjara magnetiska keramer motiveras för en förstudie. Detaljer fån ett preliminärt experiment från en högfrekvens NDT tillämpning (10 MHz)
presenteras.

NDE metoder lämpliga för karakterisering av gutet järn presenteras i kapitel fyra. Två grupper av metoder som kan användas i industriella miljöer presenteras. Dessa är metoder baserade på ultraljud samt virvelströmsmätningar. Granskningen har fokuserats på att känna av interaktionen mellan elastiska vågor och mikrostrukturen hos gutet järn. Det förklaras hur tre olika egenskaper hos ultraljud, hastighet, dämpning samt bakspridnig kan användas för karakterisering.

1. ULTRASONIC IMAGING of EB WELD

1.1   Introduction

The objective of this task is to investigate methods capable of improving ultrasonic imaging of EB-welds and more specifically, to examine algorithms based on ideas from ultrasonic tomography. Here, we present the first step in this direction.

After thorough literature review we have directed our first attempts towards methods that are base for *synthetic focusing* that can be seen as a special version of diffraction tomography [32]. The imaging algorithms have also been focused on using linear phased array systems that become more and more common in NDT applications. A linear phased array allows for (dynamic) electronic focusing in one spatial direction. In the other direction the array can be either geometrically focused at a pre-determined depth or unfocused. Dynamic focusing (focusing at more than one depth at reception) requires specialized hardware capable of handling time-dependent focusing laws. In simpler systems without this facility, several measurements must be performed with different focusing laws to obtain focusing at more than one depth.

The material presented below consists of two parts, a concise literature review in the field of inverse scattering, and report of our results obtained with synthetic focusing.

1.2   Inverse Scattering Problem – Problem Statement

The inverse problem of reconstructing an object from the scattered field is known as tomography. This inverse problem is non-linearly related to the scattering object and it is also inherently non-unique problem [1]. The nonlinear property implies that iterative procedures have to be applied to find a solution to the exact problem. In some cases it is, however, reasonable to make approximations so that the problem can be linearized. Most common approximation is to assume that the objects are small compared to the wavelength and that the object is weakly scattering, which is known as the Born approximation. By using the Born approximation one can linearize the problem and the reconstruction can be performed using efficient Fourier methods [2]. Due to the non-uniqueness of the problem one often has to choose one solution from many possible solutions.

A simple inverse scattering NDT experiment using ultrasonic transducers in immersion is shown in Figure 1. The basic idea is to use a fixed transmitter and move the receiver (a hydrophone) in a circular path to obtain ultrasonic (US) data at N angles θ and then reconstruct the object $f(r)$ from the scattering field $\Phi_s(r)$.

$$\Phi(r) = \Phi_i(r) + \int_S G_0(r,r') f(r') \Phi(r') dr' = \Phi_i(r) + \Phi_s(r) \qquad (1)$$

where $\Phi_i(r)$ is the incident field and $G_0(r)$ is the free space Green's function (when the background medium is homogeneous).

It is easy to see that if no approximation is applied the problem is nonlinear since the scattered field $\Phi_s(r)$ depends on the total field $\Phi(r)$.
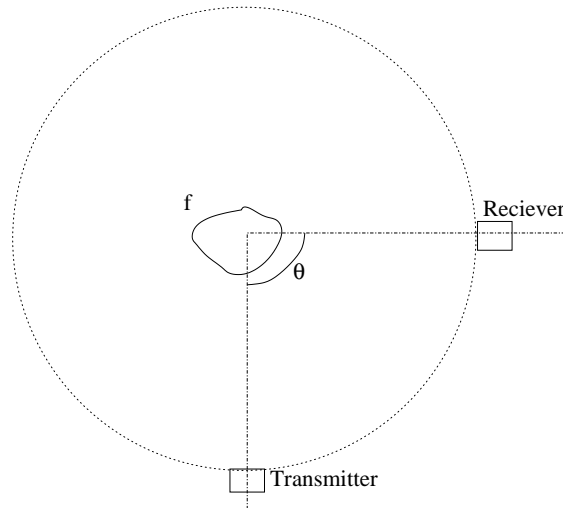

Fig. 1. Basic configuration of ultrasonic tomography.

1.3   Inverse Scattering Problem – a concise literature review

1.3.1   Weakly Scattering Media (Born Approximation)

The theory of inversion assuming week scattering, usually called *diffraction tomography* (DT), has been an open research area for about 20 years. The theory is built on linearization of eq. (1) using the Born approximation or the Rytov approximation [2]. Using the Born approximation facilitates the use of efficient fast Fourier transform (FFT) based algorithms which is due to the Fourier diffraction theorem or the generalized projection-slice theorem. Assuming the classical scan configuration where the object is insonified by a time-harmonic plane wave with wave number *k,* and the scattered field is measured along straight lines, the Fourier diffraction theorem states that the one-dimensional Fourier transform of the scattered field is mapped to a semi circular arc of radius *k* in the 2-D Fourier transform of the object *f* itself (cf. [2, 3, 4, 5] and references therein). Thus, by rotating the object the 2-D Fourier space can be filled and the object function can be found by means of the inverse 2-D Fourier transform. The most

common algorithm used in DT is the filtered back-propagation algorithm [2]. Examples of resent work where week scattering is assumed are:

- Tsihrintzis and Deveney [6] who have shown that the filtered back-propagation algorithm can be used to produce an image of the log-likelihood function for estimation of position of a known scatterer, and Tsihrintzis et al. [7] have extended this to wide-band data. They have also considered a stochastic approach [5] and derived the optimal Wiener filter solution for the linear case (first-order Born approximation).
- Dickens and Winbow have [8] have considered the resolution of diffraction tomography using different experiment geometries for geological applications.
- Anastasio and Pan [9, 10] have studied statistical properties of DT and derived algorithms for bias-free reduction of noise in reflection mode diffraction tomography (for transmission mode see refs. in [9]). In [11] Pan et al. also shows the statistical similarities between SPECT and DT imaging.

In NDT applications the probing signal is usually finite bandwidth pulses and not time-harmonic signals. Several authors have considered time-domain diffraction tomography with band-limited pulses. Pourjavid and Tretiak [12] have shown that the 3-D (and 2-D) Fourier transform of the point spread function (PSF) along a unit vector $\mathbf{u}$ is equal to the 1-D Fourier transform of the input pulse $g(t)$ scaled by a cosine of the angle of $\mathbf{u}$. That is, the bandwidth in the direction of the incident wave is maximum, while the bandwidth normal to the incident wave is zero. This implies that the reconstructed image will be distorted with a distortion that depends on the incident pulse, and the highest resolution is along the incident direction of the pulse and the lowest resolution normal to that direction. Collecting data from several directions will thus improve performance. They also state that the main limitation of time-domain diffraction tomography is imposed by the bandwidth of the incident pulse. Mast [13] has derived an efficient time-domain inversion formula that can be regarded as a generalization of confocal time-domain synthetic aperture imaging. The method is equivalent to multiple-frequency reconstructions using the filtered back-propagation algorithm, but with much greater efficiency. He also shows that the single frequency PSF has significantly greater sidelobes than the multiple-frequency ditto that implies that the multiple-frequency method has higher resolution.

1.3.2 Higher Order Born Approximation

The (first order) Born approximation is a low frequency, weak scattering, and small scatterer approximation, as mentioned in the Introduction. Several authors have extended this theory to higher order Born series. For example Lu and Zhang [14] compared first- and second-order algorithms on

simulated data with circular symmetry. The second-order algorithm out-performed the first order algorithm, but if the size of the object, or the deviation in the circular wave number, was too large the algorithms failed to reconstruct the object with good accuracy and hence, higher order algorithms must be considered.

Tsihrintzis and Devaney [4] showed that efficient FFT based algorithms could be used for computing higher-order Born series when a low-pass approximation was made for the Green's function. The resulting algorithms take the form of nonlinear data filtering followed by back-propagation. The inversion operator takes the form of homogeneous Volterra series. If the data was modeled by the first Born term all terms higher then one in the inversion operator was identical to zero. Simulations were performed using cylindrically symmetric objects with data modeled by 1-3 Born terms both with and without white noise added to the data. A comparison with a first order (linear) and a second order inversion was then performed. For first order data the to inversions where identical, but for second- and third-order data the second-order inversion algorithm outperformed the linear first-order filtered back-propagation algorithm. The second-order algorithm performed also better in the presence of noise.

1.3.3   Iterative Algorithms

Several authors have tried to improve the performance of the reconstruction, both in electromagnetic and ultrasonic scattering applications, using iterative methods. The, perhaps, most common methods are the *Born iterative method* (BIM) and the *distorted Born iterative method* (DBIM) [15, 16]. The difference between these to methods is that in the BIM method the background medium is assumed to be homogeneous while in the DBIM method the background Green's function is also updated in every iteration. Thus, in the BIM method a linear inverse problem is solved in every iteration while in the DBIM the problem can no longer be expressed in a closed form and numerical methods must be applied. The benefit of using the BIM (and DBIM) method compared to ordinary methods based on the Born approximation is that the estimate of the object function f can be used to obtain a new estimate of the internal field $\Phi(r')$ in the integral in eq. (1). The BIM method is also more robust against noise, but the DBIM method has a better performance for strong scattering objects [15].

Haddadin and Ebbini [17] have used the DBIM algorithm for imaging strong scatterers using a multiple frequency approach. The algorithm is given a starting solution using a low frequency by the Born approximation. The DBIM algorithm is then repeatedly applied for higher frequencies while checking that the algorithm does not diverge. They have also proposed a regularization method based on a singular value decomposition (SVD) to improve the robustness of the DBIM method [18].

Both the BIM and DBIM still utilize the Born approximation at every iteration step. Carfantan and Djafari [19] have instead considered a solution to the inverse problem using a Baysian framework. They

formulated the problem as finding the maximum *a posteriori* estimate that leads to a multi-modal minimization criterion.

Otto and Chew [21] have used local shape functions (LSF) for reconstructing metallic cylinder shaped objects using microwaves. The basic idea is to use small, localized functions to model arbitrary metallic objects. The algorithm solves the nonlinear inverse problem iteratively by following the linearized gradient direction in each iteration. Also, the predicted scattered field is computed in each iteration using a nonlinear multiple, scattering model. The multi-frequency version of this algorithm was able to resolve scatterers having a diameter of $0.1\lambda_{min}$ separated by a minimum of $0.51\lambda_{min}$.

Miller *et al.* [22] used B-splines to model the contour scatterers in an inhomogeneous background. The application aims at reconstructing objects located near the interface using noisy electromagnetic measurements, which is very similar to US NDT measurements. The idea is to use a low-dimensional description of the varying background and the object. They used a classical LS-criterion and two regularization factors, where the first penalized objects located too deep, and the second penalized the total length between the control points in the B-spline basis describing the objects.

1.3.4   Imaging using Array Focusing Techniques

Array focusing techniques can also be used for tomographic imaging. A group at Rochester University in New York has developed a method for focusing distributed (and point-like) objects [23, 24, 25] which can be seen as a generalization of the time-reversal mirror (TRM) technique proposed by Fink [26, 27, 28, 29]. The idea is to focus the field by re-sending, not the time-reversed original as in TRM technique, but the eigenfunctions of the scattering operator. The eigenfunctions associated with the largest eigenvalues of the scattering operator specifies the incident-wave distribution that maximizes the energy scattered to the far field by general distributed inhomogeneties as well as the point-like scatterers. The procedure can be can be implemented by iteratively retransmitting input patterns that are proportional to the measured scattered field or by numerical diagonalization. The iterative method is similar to the power method for determining eigenvectors for matrices, and the TRM method is equivalent to one, single iteration of the power method [23]. The benefit of this method for the inverse scattering problem is that the incident energy is focused on the inhomogeneities, and that the basis for expansion of the unknown medium is determined directly from scattering data. This is an advantage compared to the other methods using a fixed basis to expand the unknown medium. However, specialized hardware is required. Essentially an array transducer and electronics to transmit arbitrary waveforms is needed.

1.3.5 US Tomography and NDT

Several authors have performed research related to tomography for NDT applications. Most of them have used methods based on approximations of Eq. (1). Below are some examples:

- Rose [30] assumed that a flaw is represented with a characteristic function F(r) which is one if *r* is inside the flaw's boundary and zero if *r* is outside. Using this model he used the inverse Born approximation (IBA), both in the time and frequency domain, to determine the size, shape and orientation of the flaws. Even though the Born approximation assumes week scattering he applied the method to strongly scattering flaws such as voids and inclusions. He performed pulse-echo measurement on small well-defined voids, inclusions and cracks that were diffusion bonded titanium alloy samples with a typical size of 500μm. The results show that it is possible to characterize certain isolated flaws in metals and ceramics. In this case it was possible to determine the size, shape and orientation (of the border) given adequate experimental data.

- Kitahara at. al. [31] has compared the inverse Born approximation with the inverse Kirchhoff approximation (IKA) for a void with cercumferantial cracks. In the Kirchhoff approximation (valid in the high frequency range) a flaw is represented with a singular function $\gamma(r)$ that only takes values on the illuminated side of the surface of the object. The results show that the Born method works well for volumetric defects and that the Kirchhoff method works well for both volumetric and crack-like defects.

- Koo et al. [32] have studied the area function of voids for US tomography. They have used the fact that the impulse response from a void is the second derivative of the area function (within a multiplicative constant). The area function is the full length of the scatterer for the low-frequency approximation and the lit region of the scatterer for the high-frequency approximation. Thus, by double integrating the impulse response, known as the ramp function, and normalizing with the integral of the ramp function[1] the normalized area function is obtained which can be used to reproduce the target image. By using the area function and the Born approximation they could directly use the same existing algorithms used for X-ray CT. They used the same definition of characteristic function of the object as Rose and Kitahara. The experiments were conducted on two laboratory samples where the first was a diffusion bonded titanium block containing a spherical void and a plastic disk containing a circular copper. The results were rather good.

- Schlaberg et. al. [33] used a circular array consisting of 36 elements which had a beam angle of about 70˚. The system used digital signal processor (DSP) hardware to compute tomograms at a rate of approximately 25-30 frames per second. The used an heuristic algorithm where they match

---

[1] The integral of the ramp function is the volume of the target multiplied with the same constant.

arcs to each data item inside the target area from pulse-echo measurements. Experiments where carried out on circular objects ranging from 1.5-55 mm (results only displayed as images).

- Nielsen et. al. [34] used a 25 MHz transducer in pulse-echo mode on plexiglas and a AlSi-alloy with various radial- and axial holes and inclusions. They used the filtered back-propagation algorithm for reconstruction (i.e., Born approximation). They used a stacking technique to construct 3D imaging from the 2D tomograms. The artificial defects could be seen in the tomograms but there seem to be a substantial amount of artifacts as well.

- Malyarenko and Hinders [35] used Lamb waves and ray tracing theory (i.e., diffraction effects were ignored) to reconstruct artificial defects (flat bottom holes, through holes and rectangular thinned areas) as well as disbonded areas in aluminum aircraft structures. They used the (iterative) SIRT algorithm for the reconstruction. The performance seems rather good as long as the defects are large enough compared to the beam. For smaller defects some of the Lamb waves will interact with the defects which results in artifacts in the tomograms. The results would probably improve if diffraction effects also were considered (i.e. Lamb wave diffraction tomography).

- Hall et. al. [36] present a method, based of fuzzy logic, aimed at fusing information from reflection tomography, time-of-flight diffraction tomography, and transmission tomography. The first two methods utilized the reflected or refracted energy to reconstruct the images whereas transmission tomography uses the shadow cast by the flaw to generate defect images. The idea is to remove (or reduce) ambiguities. If, for example, planar flaws are considered the first two methods give good estimates of the defect end-points, and with the addition of transmission image it becomes possible to distinguish if the defect is two point reflectors or a planar defect. The results look promising.

1.4   Inverse Scattering - Discussion

Most of the authors treating NDT applications have used linearized approximations in their work which is rather surprising since the assumption of weak scatterers does is not valid in most NDE applications. Also linear methods (Born approximation) do not take multiple scattering into account since this as a nonlinear phenomena—the scattered field from two scatterers is not the same as the sum of the field from the individual scatterers. This results in artifacts in methods based on the Born approximation especially for objects lying close to each other. Despite the approximations made in algorithms based on the Born approximation they can be useful in imaging, for example, single small objects. That is, when the multiple scattering does not occur and only the size and position of the scatterer is interesting. However, for large, strong (multiple) scattering objects the Born approximation is not a good model. If the nonlinear problem is considered some type of regularization and low-dimensional description of the scattering objects is needed for obtaining satisfactory solutions.

1.5   *Synthetic focusing*

1.5.1   Introduction

Synthetic focusing is a technique where the focusing is performed by software after the data collection already has been performed. This technique allows for dynamic focusing using much simpler hardware. The technique can also be applied to measurements from phased array systems in directions where there is no electronic focusing or to improve focusing for array systems with no ability to perform dynamic focusing. For example, the array system can be used in an unfocused mode to electronically perform scanning of B-scan measurements and then the focusing can be performed synthetically afterwards. This results in a fast acquisition time as well as dynamic focusing. Also, the values of time-delays that are used for electronic focusing in array systems have upper and lower boundaries that limit the range where electronic focusing can be performed. Synthetic focusing can thus be an attractive alternative for situations when electronic focusing cannot be used due to these limitations.

The *synthetic aperture focusing technique* (SAFT) has been adopted from radar applications where one wanted to improve the lateral resolution in airborne radar mapping systems [37]. In these applications the transducer (i.e. radar antenna) was small – since it had to be mounted on an airplane – and the larger aperture was obtained by means coherent summations along the airplanes path. In ultrasonic applications using a small aperture transducer gives less acoustic power compared to a larger (area) transducer. This will result in more noisy measurements but the noise will be reduced when the coherent summing is performed. However, if the measurement noise becomes too severe the probe size must in general be increased. When the probe becomes larger (i.e. cannot be seen as a point source) the ultrasonic pulses will be smeared due to the spatial impulse response (SIR) of the probe [38]. If the probe becomes too large the coherent summing will no longer work since the echoes will no longer have the simple hyperbolic shape as is typical from point sources[2]. For a large probe the ultrasonic field will almost be a plane wave in the shadow of the probe and hence a hyperbolic function will fit badly resulting in over-compensated images if SAFT is applied directly. The resolution can, however, be improved if one accounts for the spatially varying SIR.

Here we will present some preliminary results from immersion testing of copper blocks using the ALLIN system in our lab facility. We have performed measurements with both small apertures (one element of the array) as well as larger apertures. In Section 1.5.2 the experimental setup the way it was used for synthetic focusing is briefly presented. Section 1.5.3 describes SAFT and Section 1.5.4 presents our approach to focusing using large apertures. Finally, Section 1.5.9 presents the results of experiments on copper blocks and Section 1.6 gives the conclusions.

---

[2] Assuming that the scanning is performed in a linear fashion in pulse echo mode.

1.5.2   The ALLIN Phased Array System for Synthetic Focusing

Our array used with the ALLIN system is a linear array is geometrically focused to 190 mm in water and consists of 64 elements. The ALLIN contains electronics enabling scanning in one dimension (no dynamic focusing). In this report we only consider two-dimensional focusing (B-scan wise), that is, the spatial extent of the sound pressure field is assumed to be small in the *x*-direction where the array is geometrically focused. This approximation has the best accuracy close to the geometrical focusing point. The array is schematically shown in Figure 2.
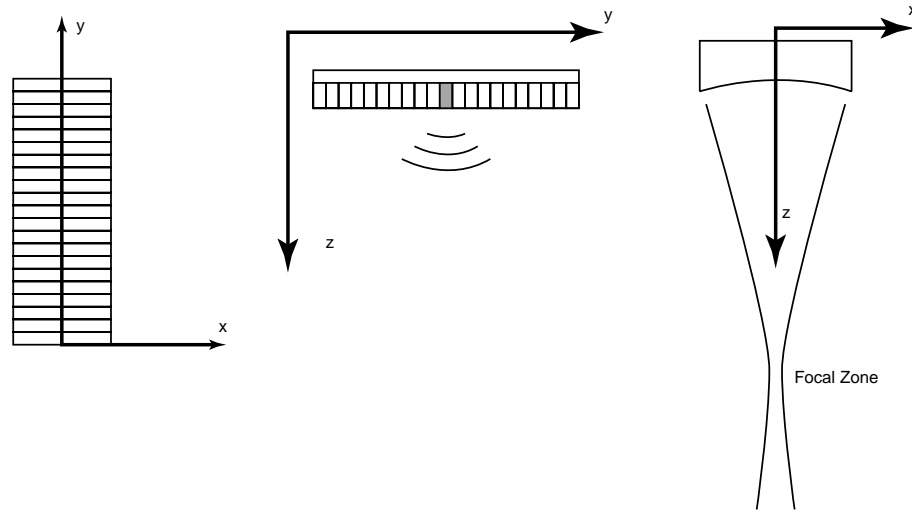

Fig. 2. Schematic view of the ALLIN array.

The reason for only considering 2D synthetic techniques is mostly practical, since 3D algorithms require more memory than is available using our present hardware. The reason for using an array system of this type is that it is very easy to change the measurement aperture (using software) still preserving the same electro-acoustical properties of the system (the same analog electronics, cables etc). If only a single element is excited, all elements of the array can be used for electronic scanning, that is, a 64 mm B-scan using the ALLIN array system in our lab. The scanning width can even be extended synthetically outside the array width with some loss of quality (see next section). If more than one element is used, the useful scanning width will decrease with the number of the used elements.[3] A more thorough description of the ALLIN system can found in [39], see also Section 1.5.9.

1.5.3   The Synthetic Aperture Focusing Technique (SAFT)

Consider a small transducer emitting spherical waves as shown in Figure 3(a). A point scatterer at the same *y*-position y_1 as the transducer and at depth z_1 will then backscatter the acoustic waves (also

---

[3] Each element is 0.9 mm wide with a spacing of 0.1 mm. The electronic scanning width is then: 64 mm – number of used elements + 1 mm.

spherical) that arrive to the transducer $2z_1/c_p$ (c_p = sound speed) seconds later. If the transducer is moved horizontally to position y_2 the backscattered wave will arrive $\sqrt{(y_2 - y_1)^2 + z_1^2}\,/c_p$ seconds later. A B-scan from such situation is shown in Figure 3(b).
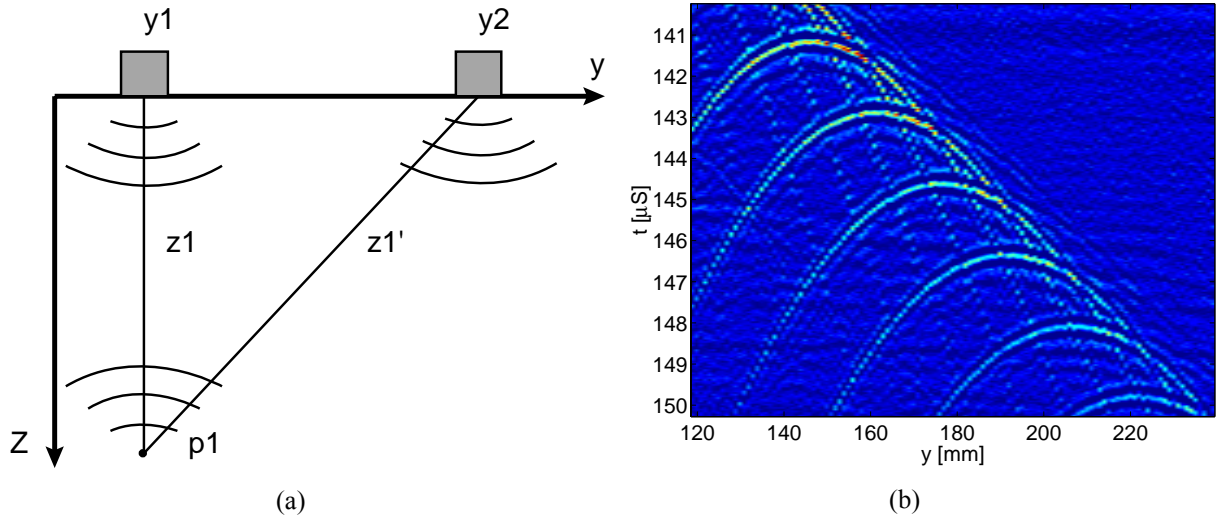

Fig. 3. (a) Sampling geometry of the immersion measurement setup. (b) B-scan from side drilled holes using one element of the array.

As can bee seen in the figure, the response from point scatterers (i.e. side-drilled holes) will exhibit the typical hyperbolic shape. The SAFT performs synthetic focusing by shifting every measurement point, $(z_1 - z_1')/c_p$ seconds, and then performing summation. That is, a coherent summation is performed for each measurement point along the hyperbolas. The synthetic aperture is determined by the maximum distance $|y_1-y_2|$ that is used in the summation. When the focusing is performed in this way, in the time-domain, the algorithm is generally referred to as the *delay-and-sum* algorithm. The computation can also be performed in the frequency domain, at least in the homogeneous case, see for example, Nagai [40] or Mayer, et al. [32]. Frequency domain algorithms are more computationally efficient but the time-domain version was easier to adapt to immersion measurements and was, therefore, chosen here.

There are some details that are worth noting when implementing the SAFT algorithm. First, the time-shifts used in SAFT are quantized by the sampling frequency used for acquisition of the ultrasonic signal. That is, the minimum delay is determined by the sampling frequency. For example, a time-shift of 1.7 samples is rounded to a two samples shift. To decrease the effect of quantized focusing in the SAFT implementation used here interpolation has been performed. For a time-shift of 1.7 samples, the sample #2 will get a weight of 0.3 and the sample #3 a weight of 0.7 in the coherent summation. Note that this is not unique for the synthetic focusing. The ALLIN phased array system has also its limitations regarding the electronic focusing. The minimum delay in the transmission is 1 ns and in the reception 25

ns (see [39]). Thus, using a higher sampling frequency than 40 MHz (= 1/25ns) ensures a lower minimum delay time for the SAFT approach compared to the ALLIN system. Second, phased arrays can be focused outside the physical aperture by adjusting the time-delays of the aperture elements properly. This can be accomplished using synthetic focusing as well. The performance will decrease however, comparing to the focusing using physical aperture since fewer A-scans will be used in the processing. That is, only parts of the hyperbolas will be used in the coherent summation process. The spatial sampling should be taken into account to avoid grating lobes, as well as the side-lobes that depend on the synthetic aperture and the apodization, see [41].

1.5.4   Synthetic Focusing using Large Apertures

The synthetic focusing procedure described above relies on spherical waves, or point sources and scatterers. If a larger transducer is used, which can not be considered as a point source, the emitted waves will no longer be spherical and the coherent summation technique will fail. Typically, if SAFT is applied to data recorded from large aperture transducers the images will look over-compensated (see Fig 11(b) in Section 1.5.10). The reason for this behavior is that in the shadow of the transducer aperture the wave field will almost be planar and, hence, a summation along hyperbolic arcs will match the field poorly. In order to analyze the problem more thoroughly the spatial impulse response (SIR) of the transducer must be considered. The SIR is the impulse response at a point $p_1 = (z_1, y_1)$ that is obtained when the transducer is at position $p_0 = (z=0, y_0)$. The SIR arise from the fact that for larger apertures the waves from different parts of the transducer surface will not arrive at the same time instant, and hence a smearing of the ultrasonic pulses will be introduced. Consider, for example, the case when point p_1 is located under the center of the transducer. In this case the first wave arriving at point p_1 originates from the center point of the transducer and the last wave originates from its edge. Thus, the SIR will be a spatially varying filter that smears the ultrasonic pulse emitted from the surface of the transducer. If the geometry of the transducer is symmetric with respect to the center of the transducer the SIR:s will also be symmetric with respect to the center line. In discrete time, the SIR:s will basically be a FIR (finite impulse response) filters with all coefficients ≥ 0.

To successfully perform synthetic focusing the smearing due to the SIR:s must be considered. If linear methods are considered the "de-smearing" or deconvolution filter must be a non-stationary one since the SIR:s are non-stationary. The approach chosen here consists in using a linear model for the system and performing the 2D deconvolution by means of a non-stationary Wiener filter realized in time-domain. This model accounts for the smearing due to the SIR:s but effects such as multiple scattering are not considered.

1.5.5 Numerical Algorithm for Computing the Spatial Impulse Response in an Immersed Solid

The ALLIN array system consists of narrow strip-like elements that are focused geometrically at 190 mm. The elements are 0.9 mm wide and there is a small gap of 0.1 mm between each element. The spatial impulse response of this type of cylindrically concave array has been calculated by Wu and Stepinski using a semi-numerical algorithm [42]. They did, however, not consider immersed solid. When calculating the SIR for the immersed solids one has to take the Snell's law into account in the water-solid interface. Here, an approximate numerical algorithm has been used to calculate the SIR:s for immersed solids. Two approximations have been introduced. The first one consisted in neglecting the small space between the array elements so that the array can be seen as a single rectangular transducer, geometrically focused in the x-direction and unfocused in the y-direction. The second approximation was the assumption that the SIR is two-dimensional only which is a reasonable assumption close to the geometrical focus where the field is very narrow in the x-direction. The SIR was then calculated directly in a sampled-discrete form based on the calculation of the area of the probe that is active during each sampling interval[4]. To understand the principle let us consider two consecutive sampling instants t_n and t_{n+1}. These sampling instants correspond to two points on the transducer surface (using Snell's law for a spatial point p). The SIR for this particular point is then the distance between the points on the transducer surface for all t_n. This is illustrated in Figure 4 where the spatial sampling points are marked with dots.
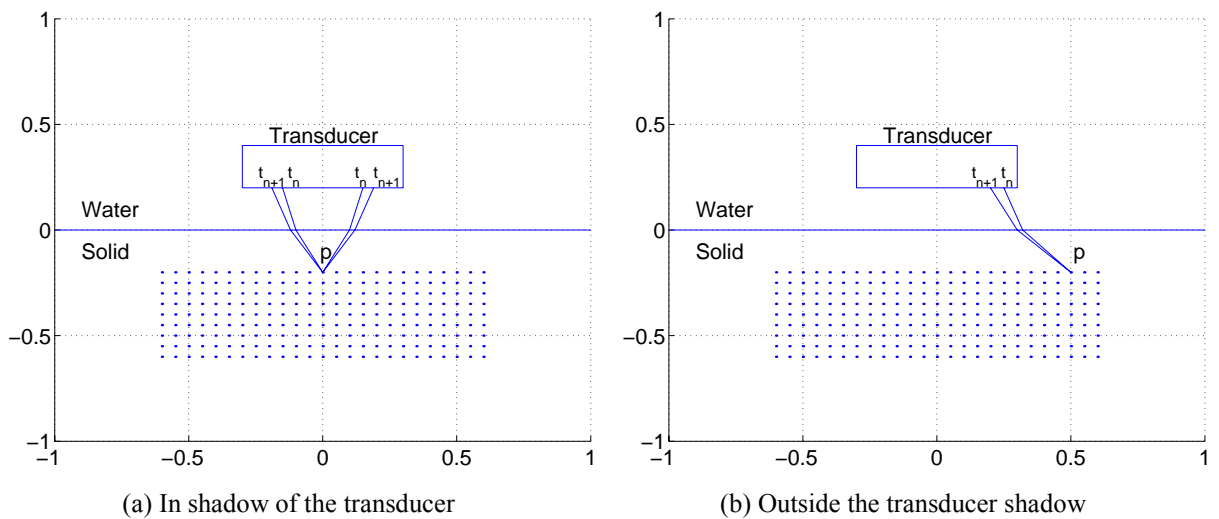

(a) In shadow of the transducer   (b) Outside the transducer shadow

Fig. 4. Illustration of the probe areas active in a particular sampling interval [t_n t_{n+1}].

---

[4] Since the width in the x-direction is the same for all elements only the width in y-direction is used in reality.

Note that the respective area is twice as large if the spatial point is in the shadow of the transducer (Figure 4(a)) compared to when the spatial point is outside the shadow (Figure 4(b)). That is, the ultrasonic wave will now have a more focused shape instead of the spherical shape which small aperture transducers described in Section 1.5.3 have.

Figures 5 and 6 show the SIR:s at different positions for an immersed copper block, where the transducer was placed 92 mm above the water-copper interface ($y=0$ means that the spatial point is centered under the transducer).
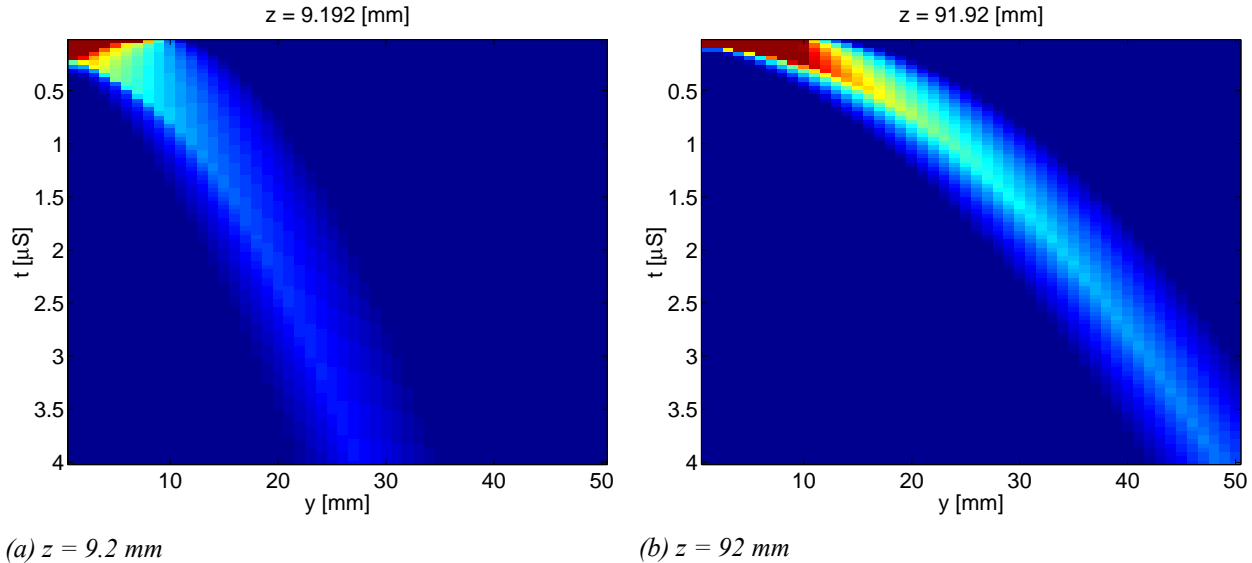

(a) z = 9.2 mm

(b) z = 92 mm

Fig. 5. Echoes from a plane surface of an immersed copper block and a 16 mm aperture at two fixed depths (z is the distance from the water-copper interface).
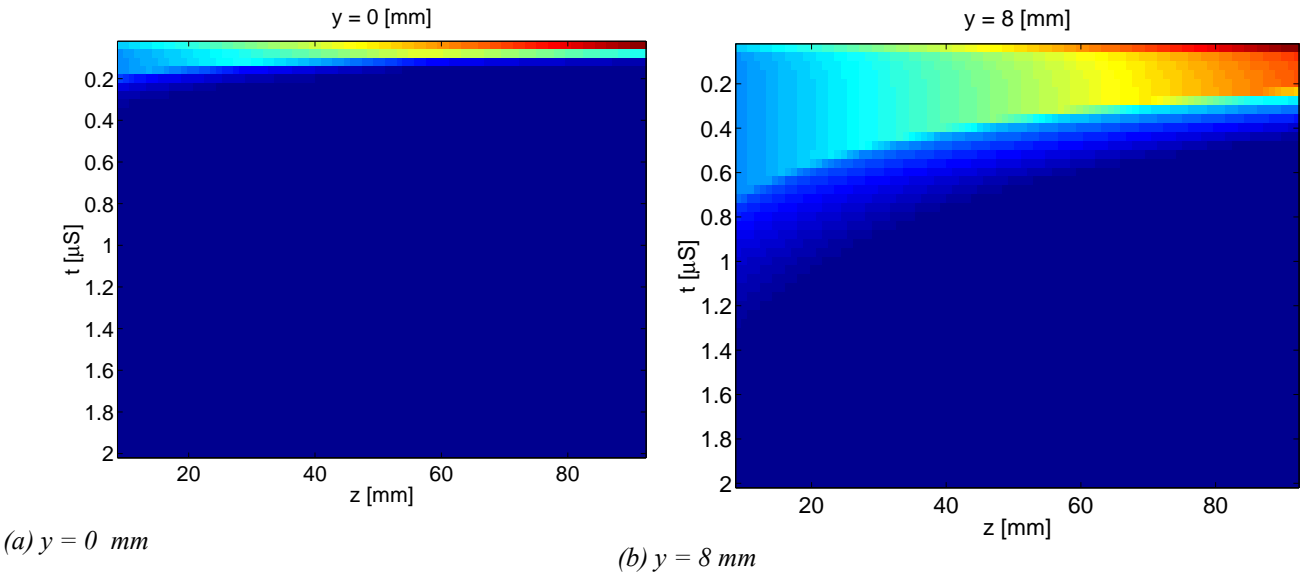

(a) y = 0 mm

(b) y = 8 mm

1-13

Fig. 6. Spatial impulse responses for an immersed copper block and a 16 mm aperture at fixed *y*-positions.

Note that the SIR:s obtained at a spatial point located close to the transducer have a longer duration and, hence a more low-pass character, than the ones measured at the point located far away. Note also the that SIR:s drop off fast outside the transducer aperture (red color corresponds to a high amplitude and blue is a low amplitude).

1.5.6   The Electro-acoustical Impulse Response

So far, we have only considered the effects of the SIR and not the effects of the electro-acoustical properties of the measurement system. This is what is normally referred to as the system impulse response and is determined by the piezo-electric crystal in the probe, the excitation pulse, the cables, amplifiers etc. The total impulse response will then be the combination of both the SIR and the electro-acoustical impulse response (EAIR). It is in general difficult to obtain the EAIR without performing measurements.

In [43] flat-bottom holes (FBH) were used as prototypes for the impulse response. The SIR was not considered and the impulse response is, therefore, a combination of the SIR the EAIR as well as effects that result from the shape of the FBH and the fact that the measurements where performed in immersion. This is a reasonable approach if the only objective is to improve the temporal resolution at fixed depths such as the EB-weld [43]. Here we have, however, adopted the same technique as in [42] to obtain the EAIR. This was done to obtain an impulse response that does not depend on the SIR. In short, measurements have been performed on a small steel pin using 16 elements of the array and then the SIR for this aperture has been deconvolved using Wiener-filtering techniques. Figure 7 shows the measured and the deconvolved electro-acoustical impulse response. From Figure 6 it can be seen that both curves are pretty similar (a time shift that has been introduced to facilitate the comparison).
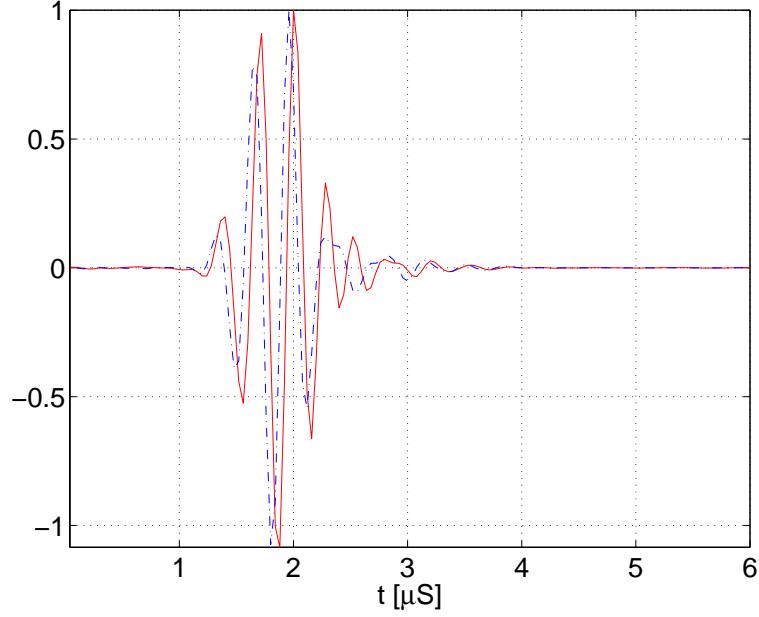
Fig. 7. Electro-acoustical Impulse Response. Blue-dash-dotted: measured response, Red-Solid: SIR deconvolved response (the impulse responses have been separated slightly for clarity).

1.5.7 The Inverse Filter

The measurement system is modeled as a linear system where the measurements (A-scans) result form the superposition of the responses from small scatterers. Let *O(z,y)* denote the *object function* which describes the position of these scatterers. If an infinite bandwidth point transducer is used then the an A-scan measurement would simply be a sum of time-delayed Dirac functions, where *O(z,y)* gives the time delays. In reality the SIR:s and the EAIR will filter this response, so the response will not have this simple form.

The object function is sampled at K×N spatial points and denoted **O**. Let $\mathbf{o}_i$ be column *i* in **O**. Then an A-scan measurement $\mathbf{x}_k$ can be written

$$\mathbf{x}_k = \mathbf{H} \sum_{i=-M+k}^{M+k} \mathbf{S}_{|i-k|} \mathbf{o}_i + \mathbf{e}_k \tag{1}$$

where *k* is the A-scan index (k=1,2,…,K), *M* half the synthetic aperture (*N* is the length of the A-scans), and $\mathbf{e}_k$ is the measurement noise combined with modeling errors (assumed to be white Gaussian). The matrix **H** is a N× N toeplitz matrix containing the electro-acoustical impulse response, and the N×N matrices $\mathbf{S}_{|i-k|}$ contain the SIR:s ($|i-k|=0$ means that $\mathbf{o}_i$ is under the center of the transducer). Figure 8 shows the simulated response for a point scatterer when the EAIR is neglected (i.e., **H = I,** where **I** is the identity matrix). Note that the response differs significantly from the hyperbolic response that is assumed in the SAFT algorithms.
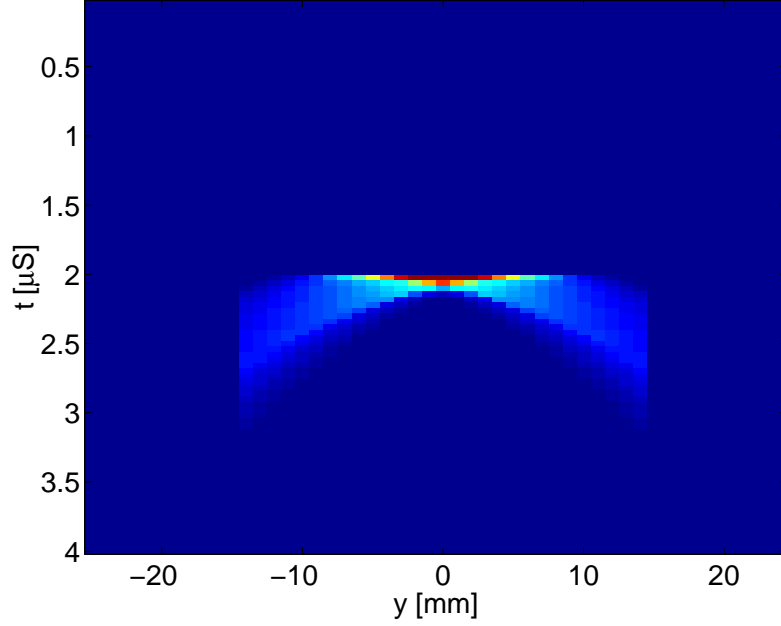
Fig. 8. Simulated response obtained for a point scatterer at z = 50.5 mm below water solid interface for a 16 mm aperture (synthetic aperture M= 29 mm).

Note also that *2M-1* vectors $\mathbf{o}_i$ are used in the summation in Eq (1). That is, each A-scan is a sum of several vectors $\mathbf{o}_i$. In order to get good estimates of $\mathbf{o}_i$ the number of A-scan:s used in the processing must be at least be as many as the $\mathbf{o}_i$ otherwise the problem becomes underdetermined resulting in poor performance. The model Eq (1) is, therefore, extended by stacking several A-scan:s and $\mathbf{o}_i$:s in column vectors $\mathbf{x}$ and $\mathbf{o}$ respectively, according to Eq. (2)

$$x = H_0 So + e \tag{2}$$

The matrices $\mathbf{H}_0$ and $\mathbf{S}$ are now large block-matrices with $\mathbf{H}$ and $\mathbf{S}_{|i-k|}$ on the respective diagonals. The inverse problem of finding $\mathbf{o}$ from measurements $\mathbf{x}$ can now be formulated. First the sampled object function and the measurement noise are modeled as white Gaussian processes with zero mean and covariance matrices $\mathbf{C}_{oo}$ and $\mathbf{C}_{ee}$ respectively. The problem is then formulated as a search for a matrix $\mathbf{K}$ that minimizes the mean squared error

$$J = E\{\|o - Kx\|^2\} = tr\{C_{00}\} - 2tr\{KH_0 SC_{00}\} + tr\{K(H_0 SC_{00}S^T H_0^T + C_{ee})K^T\} \tag{3}$$

where $tr\{\cdot\}$ is the trace operator.

The matrix $\hat{K} = arg\,\underset{K}{min}\,J$ that minimizes the criterion (3) is the classical Wiener filter

$$\hat{K} = C_{ee}S^T H_0^T (H_0 SC_{00}S^T H_0^T + C_{ee})^{-1} \tag{4}$$

Since both $\mathbf{o}$ and $\mathbf{e}$ are white Gaussian sequences their covariance matrices are diagonal $C_{00} = \lambda_0 I \quad and \quad C_{ee} = \lambda_e I$. The ratio between λ_0 and λ_e determines the regularity of the solution. If,

for example, the measurement noise variance, λ_e, is high the diagonal matrix $\boldsymbol{C}_{ee}$ will dominate in the inverse in Eq. (4) resulting in a smooth reconstruction. If the noise level is low the inverse is dominated by the factor $\boldsymbol{H}_0 \boldsymbol{S} \boldsymbol{C}_{00} \boldsymbol{S}^T \boldsymbol{H}_0^T$ which means that more weight will be given to the measurements. The ratio λ_e / λ_0 can be seen as a tuning parameter which can be altered to trade between confidence in the measurements and the regularity (i.e. bias and variance). The matrices in Eq. (4) are very large, but they are also sparse. This fact can be utilized when computing $\hat{\boldsymbol{K}}$. Common software packages like MATLAB$^{\text{TM}}$ have support for computing sparse matrix inverses etc. Without this facility, the inversion the matrix in Eq. (4) would be intractable using our present hardware. The computation of the Wiener filter matrix $\hat{\boldsymbol{K}}$ is still rather computationally demanding. This matrix can, however, be pre-computed and the deconvoultion is then performed using a simple matrix-vector multiplication than can be performed very efficiently.

1.5.8   Approximate Inverse Filter

Despite that sparse matrix tools were used for the calculations the optimal solution (4) to Eq. (3) is still too demanding computationally. The problem is that $\mathbf{H}_0$ makes Eq. (4) less sparse. That is, $\mathbf{H}_0\mathbf{S}$ contains more non-zero entries than $\mathbf{S}$. An approximate solution is to separate the deconvolution of the EAIR and the SIR in two steps. Then one can use $\mathbf{H}$ instead of $\mathbf{H}_0$ for deconvolving the EAIR, which is a much smaller problem. The two-step deconvolution can be accomplished in two ways, by deconvolving the EAIR first and the SIR afterwards or vice verse. The order of this procedure may have some influence on the final result since $\mathbf{H}$ is measured and $\mathbf{S}$ is computed by a numerical algorithm. That is, $\mathbf{H}$ has measurement (and modeling) errors and $\mathbf{S}$ has modeling errors that are different and enter differently depending on the order of the two deconvolutions. This topic is presently under investigation.

1.5.9   Experiments

In this section some preliminary results are shown obtained using the ALLIN system in our lab for the inspection of two immersed copper blocks, the first made of solid copper with side-drilled holes and the second a EB-welded block with natural defects. The water column used was approx. 92 mm which gives that the geometric focus approx. 30 mm in copper. A schematic diagram of the measurement setup is shown in Figure 9.
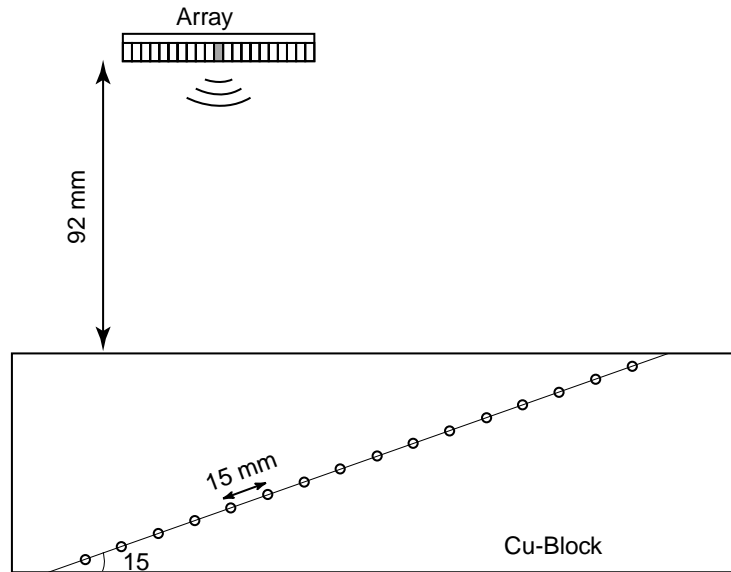
Fig. 9. Measurement setup.

The side-drilled holes (SDH) are 1 mm in diameter and are separated 15 mm and drilled in a line inclined with an angle of 15 degrees. The scanning has been performed in the *y*-direction giving B-scans of 250 mm.[5]

1.5.10 Synthetic Aperture Focusing Technique on Immersed Copper Blocks

The SAFT algorithm has been tested using the test block shown in Figure 9 and an EB-welded Cu-block. Measurements have been performed using one element of the array as well as 16 elements. When 16 elements was used all elements were fired at the same time-instant (no focusing law was applied). Two B-scan:s using 1 and 16 elements respectively are shown in Figure 10.

(a) 1 element

(a) 16 elements

Fig. 10. B-scans from side drilled holes.

---

[5] The separation between each A-scan was 1 mm.

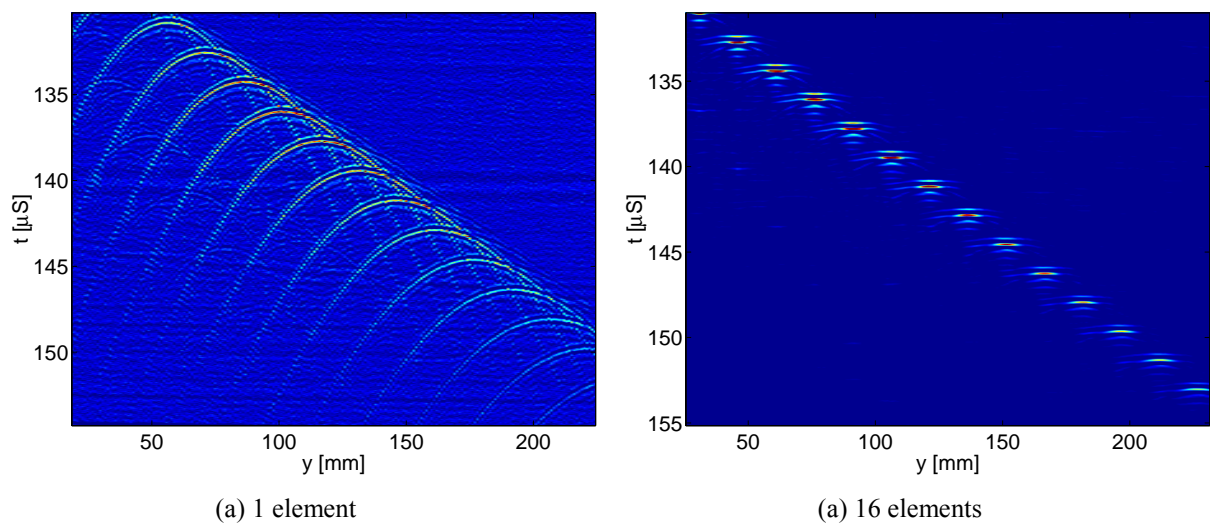It is easy to see that the 16-element aperture results in a much narrower beam pattern than the 1-element ditto. It is also easy to see that the distinct hyperbolic pattern in Figure 10(a) is much less pronounced in Figure 10(b).

The idea behind using one element only is to compare the performance of the SAFT algorithm to the measurements obtained with focused array. One element is not strictly a line-segmented transducer, it has a width of 0.9 mm, but it is the smallest aperture available for the array. However, it behaves approximately as a point transducer that can be seen in Figure 10(a). The SAFT algorithm was also applied to the measurements shown in Figure 10(b) where a larger aperture has been used (16 mm). This was done in order to investigate the behavior of SAFT processing when small aperture transducers are not available or when the signal to noise ratio is too poor to use a small aperture. The processed B-scan data in Figure 10 are shown in Figure 11 where a synthetic aperture of 31 mm has been used.

(a) 1 element   (b) 16 elements
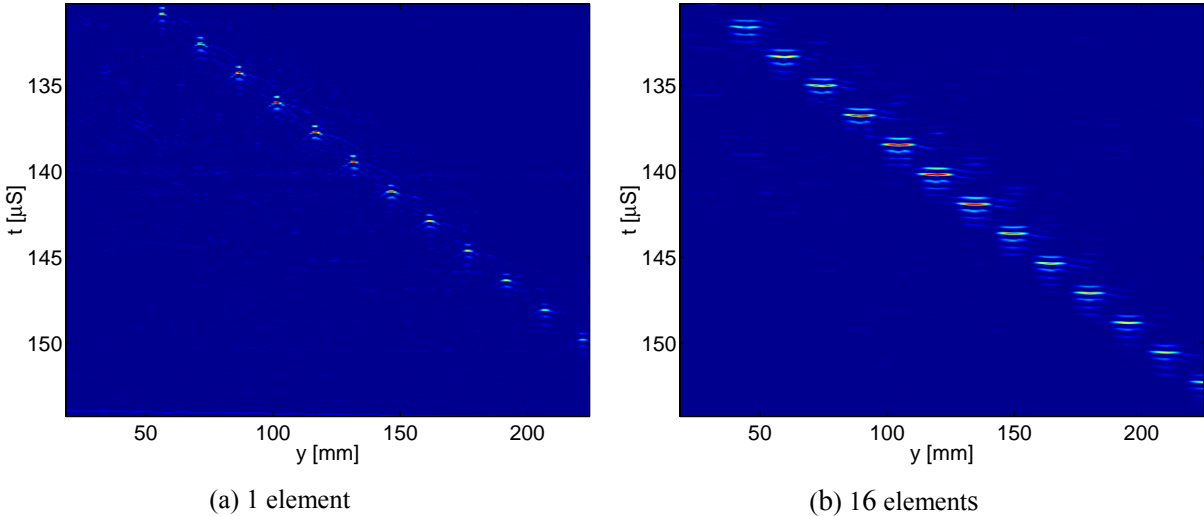
Fig. 11. SAFT processed B-scans of side drilled holes.

The SAFT algorithm applied to the data using 1-element shows a significant increase in spatial resolution as well as better signal to noise ratio. The temporal resolution is, however, about the same as in the original measurement, which is not surprising since it should not be affected by the SAFT algorithm. For comparison a measurement using 32-element focused at approximately 30 mm in copper is shown in Figure 12. The aperture of 32 elements was chosen so that both the focused and the synthetic aperture would have the same size and could be compared. Both the temporal and the spatial resolution is approximately the same in Figure 11(a) and Figure 12.
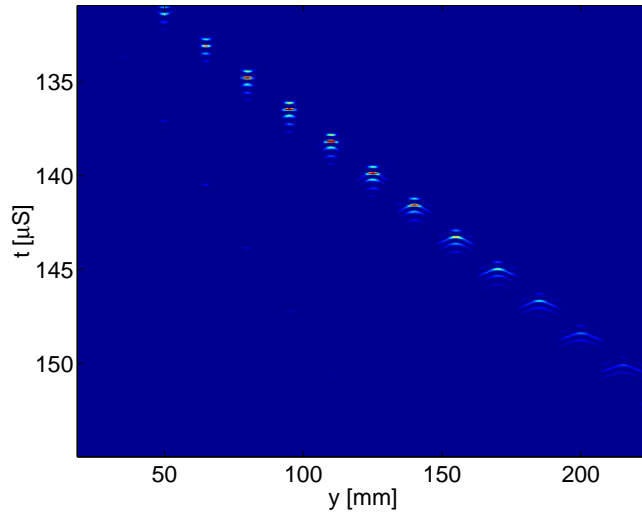
Fig. 12. B-scan measurement with a focused array using 32 elements.

The SAFT processed data is focused in the whole B-scan. This, however, is not the case for the 32-element physical focused aperture. Figure 11(b) shows the SAFT algorithm applied to data using 16-elements shown in Figure 10(b). The resolution is nearly the same as the original measurement and a slightly over-compensated behavior can be observed (the response from the SDH:s bends slightly upwards instead of downwards). This result indicates that the aperture size must be considered before applying the SAFT algorithm. Using the SAFT algorithm on too large aperture will otherwise lead to poor performance.

Figure 13 shows an additional comparison of SAFT and electronic focusing using 32 elements of the EB-welded Cu-block TB25b. The block has been inspected from the top-side in the same manner as the CAN1 block [42].

Focused using 32-elements.

SAFT using a synthetic aperture of 31 mm.

Fig. 13. C-scans from the Cu-block TB25b.

1-20

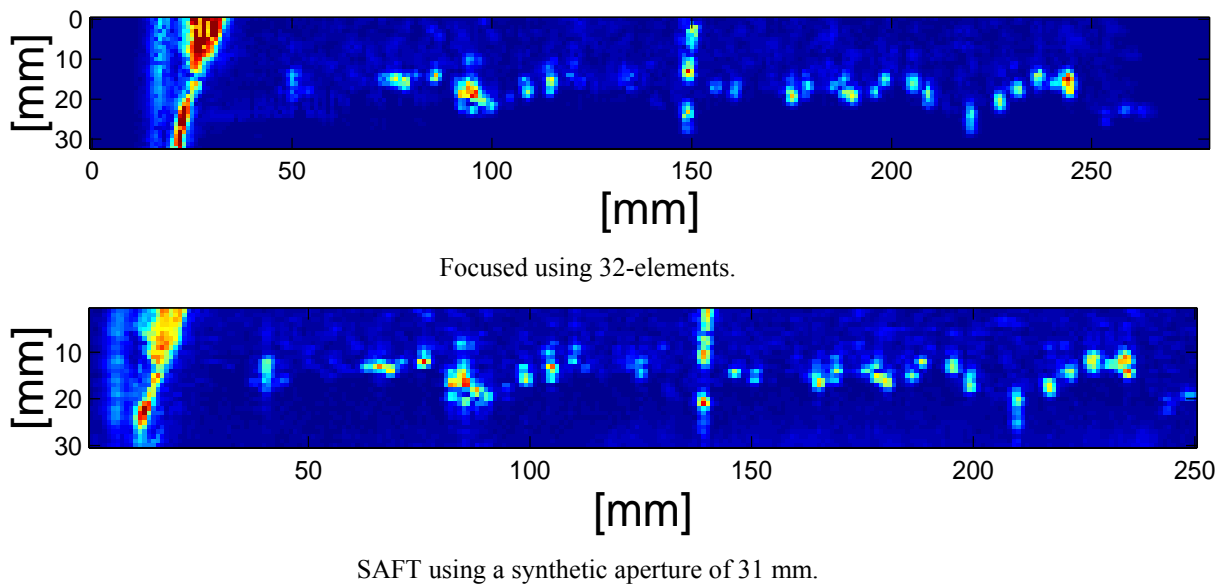The C-scans in Figure 13 are computed by taking the max amplitude of the signals within the time gate covering the EB weld layer. From Figure 13 it can be seen that the performance is nearly identical using both techniques. The difference is that when using the SAFT method the electronic scanning can be performed for 64 mm instead of the 32 mm which can be obtained for the 32 element focused case. This will improve the acquisition speed since the electronic scanning is much faster then the mechanical scanning.

1.5.11 Deconvolution of the Spatial Impulse Response

In this section we consider deconvolution of the spatial impulse response only. That is, we concentrate on increasing the spatial resolution and disregard the temporal deconvolution. As mentioned in Section 1.5.8 temporal deconvolution can be performed both before and after spatial (SIR) deconvolution and is regarded as a separate issue.

The SIR-Wiener deconvolution has been performed on measurements using (un-focused) data from an aperture of 16 mm (i.e. 16-elements). The original measurements and the processed results are shown in Figure 14. The matrices involved in the computation become very large for large B-scans. The B-scans has, therefore, been cut into smaller parts and it is these smaller B-scans that have been SIR-Wiener deconvolved. The large B-scan in Figure 14(b) has been created by pasting those small B-scans together afterwards. This may result in some small temporal edge effects at the block borders. This can, however, be avoided by using overlapping blocks.
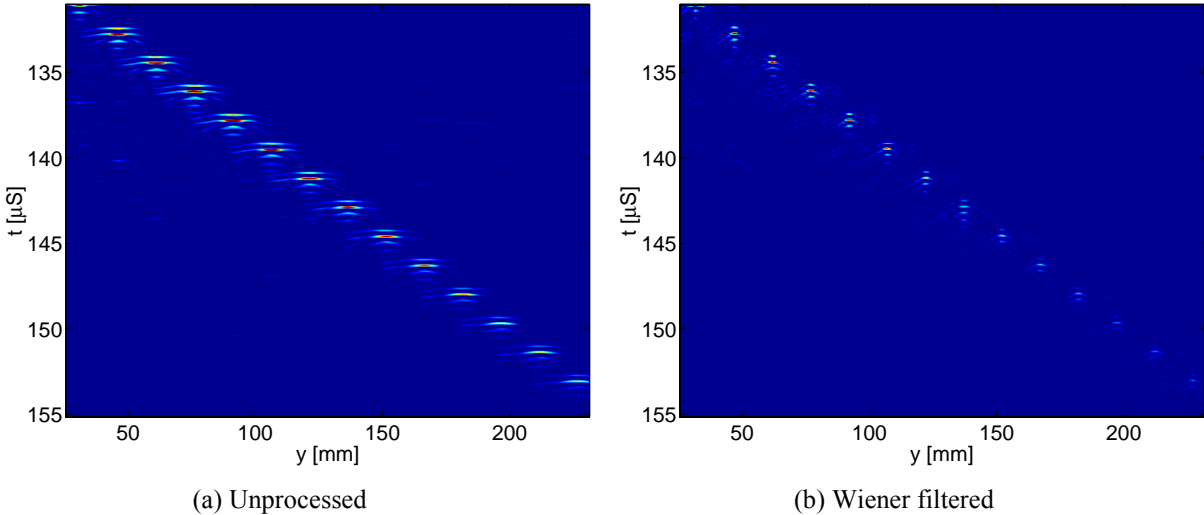

(a) Unprocessed   (b) Wiener filtered

Fig. 14. SIR deconvolution of B-scan data from side-drilled holes (16 elements).

The result shown in Figure 14(b) has a spatial resolution comparable with the SAFT algorithm using 1-element data and the 32-element focused data. [6] Thus, this technique is very promising for the situations when the signal to noise ratio is too poor for using the classical SAFT algorithms or when dynamic (time-dependent) focusing is not available. Another benefit is that much simpler hardware can be used since the full array system is not needed. It can also be used to improve resolution of the arrays that cannot be geometrically focused (e.g. used in contact inspection). This can, for example, be accomplished by using the array to perform electronic focusing in the *y*-direction and then perform SIR-deconvolution in the *x*-direction. If this is repeated for several depths 3D-data with high resolution in both *x*- and *y*-direction can be obtained.

It must, however, be stressed that the above reported research is still in an early stage and there are many issues that remain to be investigated, for example, how is the SAFT performance influenced by the measurement aperture, transducer bandwidth, modeling errors etc.

1.5.12 Deconvolution of the Temporal Impulse Response

Deconvolution of the temporal impulse response, or the electro-acoustical impulse response, is much less computationally demanding than the SIR deconvolution since in only involves 1D computations and the inversion filter is stationary. The problem here is that the EAIR must be obtained by measurements that contain several types of measurement errors. The method used to obtain the EAIR is briefly described in Section 1.5.6, and typical sources of errors are: the measurement noise, mechanical errors due to the scanning procedure, the fact that the object that is used to measure the EAIR is not strictly a point scatterer, etc. Figure 15 shows one example, where measurements from SDH:s have been deconvolved using the procedure described above.
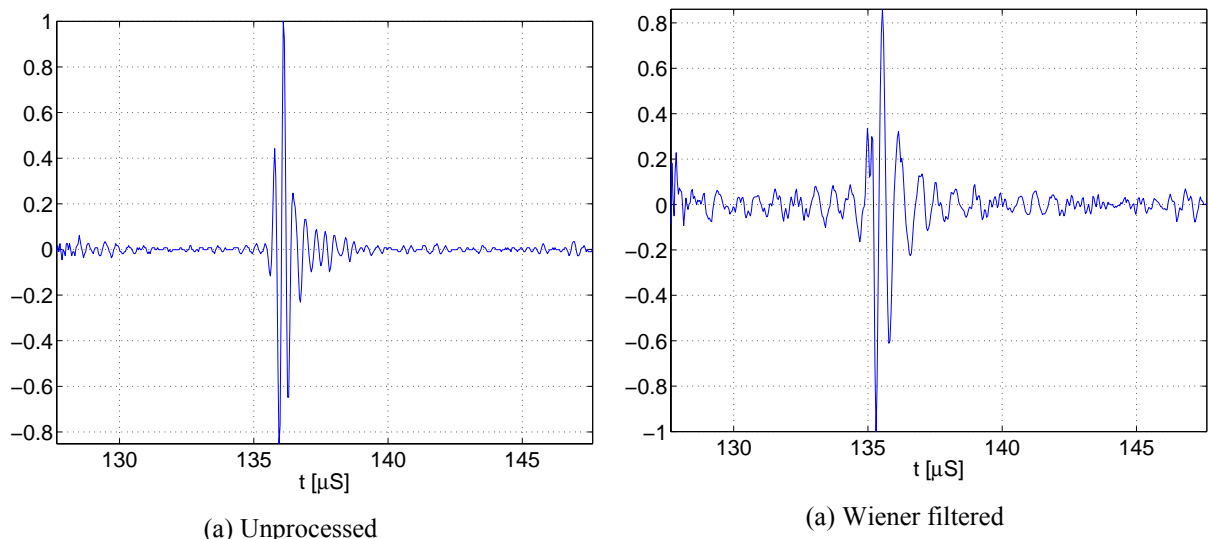

| (a) Unprocessed | (a) Wiener filtered |

Fig. 15. Temporal deconvolution of A-scan data from a side-drilled hole (16 elements).

---

[6] That is, when the SDH:s is in the focal zone for the 32-element focused measurements.

As can be seen the temporal resolution has not been increased by this procedure. The duration of the pulse is approximately the same before and after processing, the pulse is however more low-frequent than the original measurement. The reason for this might be that SDH:s does not have the same ultrasonic response as a point scatterer, hence the deconvolution does not result in a short Dirac pulse. This topic is currently under investigation with the aid of simulation software for ultrasonic scattering such as UT-Defect [44].

If a short response is desired for SDH:s a SDH can be used as a prototype instead of the method used above. The result from such an experiment is shown in Figure 16. Clearly, a high temporal resolution for SDH:s has been obtained.

(a) A-scan at y = 76 mm.

(a) B-scan
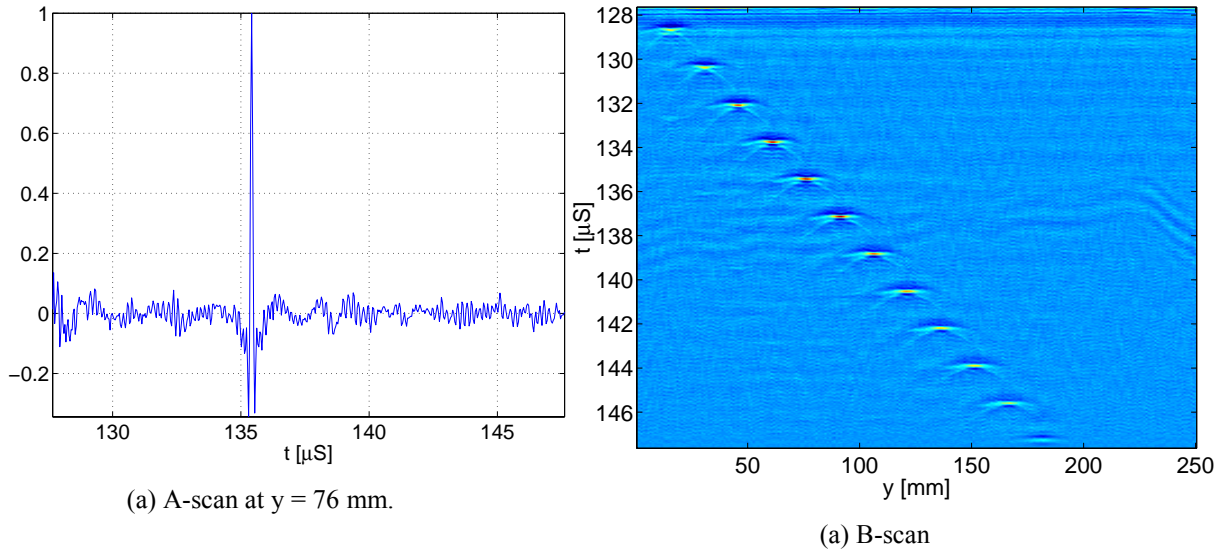
Fig. 16. Temporal deconvolution of data from side-drilled holes (16 elements) with a SDH used as prototype.

Note also that the noise level increases when performing deconvolution. This can be controlled, as mentioned in Section 1.5.7, by the noise factor in the Wiener filter. However, there is always a trade-off between resolution and noise level.

1.6   Conclusions

In evaluation of backscattered data from ultrasonic inspections important issues are to detect, locate, and size defects in the region of interest. The imaging system, that is, the probe, scanning mechanics, amplifiers, cables etc., will influence the measurements, which makes it more difficult for an operator to perform the evaluation. Typically, the operator must learn how the imaging system "distorts" the measurements in order to be able to make adequate decisions. Two factors that have a large

influence are the electro-acoustical impulse response of the system and the spatial impulse response of the used probe. These two factors will smear the results making the data more difficult to evaluate. The spatial impulse response makes the evaluation especially difficult since the smearing effect varies with the location of the defect.

The two signal processing techniques, SAFT and 2D Wiener deconvolution discussed here can be of great aid in NDE applications. The technique, which is most suitable to use, depends on a particular application, that is, the type of hardware, that is used, and the properties of the inspected material. Since in the Cu-blocks, which have been used here for testing, the level of backscattering from grains (material noise) is low both methods performed equally. The resolution was at least as good as the one obtained using a focused phased array of similar aperture.

The main benefit of using the synthetic methods is that the processed data can be focused for all depths, while a focused phased array has a fixed focal zone. The synthetic methods may be the only alternative if the unfocused transducers have to be used for some reason. The synthetic methods can be also used in a phased array system for improving the electronic focusing limited by the aperture size. The two latter cases are of significant interest for the canister inspection.

1.7 References

[1]   W.H. Chew. *Waves and Fields in Inhomogeneous Media.* IEEE Press, 1995.

[2]   A.C. Kak and M. Slaney. *Principles of Computerized Tomographic Imaging.* IEEE Press, 1988.

[3]   B.A. Roberts and A.C. Kak. Reflection mode diffraction tomography. *Ultrasonic Imaging,* 7(4) , pp.300- 320, 1985.

[4]   G.A. Tsihrintzis and A.J. Devaney. Higher-order (nonlinear) diffraction tomography: reconstruction algorithms and computer simulation. *IEEE Transactions on Image Processing,* 9(9), pp.1560-1572, Sept 2000.

[5]   G.A. Tsihrintzis and A.J. Devaney. Stochastic diffraction tomography: theory and computer simulation. *Signal Processing,* 30(1) , pp.49-64, 1993.

[6]   G.A. Tsihrintzis and A.J. Devaney. Application of a maximum likelihood estimator in an experimental study in ultrasonic diffraction tomography. *IEEE Transactions on Medical Imaging,* 12(3) , pp.545- 554, 1993.

[7]   G.A. Tsihrintzis, A.J. Devaney and E. Heyman. Estimation of object location from wideband scattering data. *IEEE Transactions on Image Processing,* 8(7), pp.996-1001, July 1999.

[8]   T.A. Dickens and GA. Winbow. Spatial resolution of diffraction tomography. *Journal of the Acoustical Society of America,* 101(1), pp.77-86, Jan 1997.

[9]   M.A. Anastasio and X. Pan. A new reconstruction approach for reflection mode diffraction tomography. *IEEE Transactions on Image Processing,* 9(7), pp.1262-1271, July 2000.

[10]   X.Pan and M.A. Anastasio. A novel approach for a bias-free reduction of image variance in ultra-sonic diffraction tomograph. In *IEEE Ultrasonics Symposium. Proceedings (Cat. No.*

98CH36102), volume 2, pp. 1627-1630, 1998.

[11] X.Pan, M.A. Anastasio and C.M. Kao. A comparative study of image reconstructions in spect and ultrasonic diffraction tomography. *IEEE Transactions on Nuclear Science,* 46(3) , pp.527-534, June 1999.

[12] S. Pourjavid and 0. Tretiak. Ultrasound imaging through time-domain diffraction tomography. *IEEE Transactions on Ultrasonics, Ferroelectrics and Frequency Control,* 38(1), pp.74-85, Jan 1991.

[13] T.D. Mast. Wideband quantitative ultrasonic imaging by time-domain diffraction tomography. *Journal of the Acoustical Society of America,* 106(6), pp.3061-3071, Dec 1999.

[14] Z.Q. Lu and Y.Y. Zhang. Acoustical tomography based on the second-order born transform perturbation approximation. *IEEE Transactions on Ultrasonics,* 43(2) , pp.296-302, March 1996.

[15] W.C. Chew G.P. Otto W.H. Weedon J.H. Lin C.C. Lu Y.M Wang and M. Moghaddam. Nonlinear diffraction tomography—the use of inverse scattering for imaging. *International Journal of Imaging Systems and Technology,* 7(1), pp.16-24, 1996.

[16] W.C. Chew and Y.M. Wang. Reconstruction of two-dimensional permittivity distribution using the distorted. *IEEE Transactions on Medical Imaging,* 9(2), pp.218-225, June 1990.

[17] O.S. Haddadin and E.S. Ebbini. Imaging strongly scattering media using a multiple frequency distorted born iterative method. *IEEE Transactions on Ultrasonics, Ferroelectrics and Frequency Control,* 45(6), pp.1485-1496, Nov 1998.

[18] O.S. Haddadin and E.S. Ebbini. Adaptive regularization of a distorted born iterative algorithm for diffraction tomography. In *Proceedings. International Conference on Image Processing (Cat. No.96CH3591 9). IEEE, New York, NY, US,* pp. 725-728, 1996.

[19] H. Carfantan and A. Moharnmad-Djafari. A bayesian approach for nonlinear inverse scattering tomographic imaging. In *ICASSP-95, International Conference on Acoustics, Speech, and Signal Processing,* volume 4, pp. 2311-2314, 1995.

[20] H. Carfaatan, A. Mohammad-Djafari and J. Idier. A single site update algorithm for nonlinear diffraction tomography. In *IEEE International Conference Acoustics, Speech, and Signal Processing ICASSP-97,* volume 4, pp. 2837-2840, 1997.

[21] G.P. Otto and W.C. Chew. Microwave inverse scattering-local shape function imaging for improved resolution of strong scatterers. *IEEE Transactions on Microwave Theory and Techniques,* 42(1), pp.137- 141, Jan 1994.

[22] E.L. Miller, M. Kilmer and C. Rappaport. A new shape-based method for object localization and characterization from scattered field. *IEEE Transactions on Geoscience and Remote Sensing,* 38(4), pp.1682- 1696, 2000.

[23] T.D. Mast, A.I. Nachman and R.C.Waag. Focusing and imaging using eigenfunctions of the scattering operator. *Journal of the Acoustical Society of America,* 102(2), pp.715-25, 1997.

[24] T.D. Mast, A.I. Nachman D.L. Liu and R.C. Waag. Quantitative imaging with eigenfunctions of the scattering operator. In *IEEE Ultrasonics Symposium Proceedings (Cat. No.97CH36118),* volume 2, pp. 1507-1510, 1997.

[25] F. Lin A.I. and Naohmanand R.C. Wang. Quantitative imaging using a time-domain eigenfunction method. *Journal of the Acoustical Society of America,* 108(3), pp.899-912, Sept 2000.

[26] M. Fink. Time-reversal mirrors. *Journal of Physics D (Applied Physics),* 26(9), pp.1333-1350, Sept 1993.

[27] M. Fink. Time reversal of ultrasonic fields. I. Basic principles. *IEEE Transactions on Ultrasonics, Ferroelectrics and Frequency Control,* 39(5), pp.555-566, Sept 1992.

[28] F. Wu, J.L. Thomas and M. FinkM. Time reversal of ultrasonic fields. II. Experimental results. *IEEE Transactions on Ultrasonics, Ferroelectrics and Frequency Control,* 39(5) , pp.567-578, Sept 1992.

[29] D. Cassereau and M. Fink. Time-reversal of ultrasonic fields. III. Theory of the closed time-reversal cavity. *IEEE Transactions on Ultrasonics, Ferroelectrics and Frequency Control,* 39(5), pp.579-592, Sept 1992.

[30] J.H. Rose. Elastic wave inverse scattering in nondestructive evaluation. *Pure and Applied Geophysics,* pp. 515-739, 1989.

[31] M. Kitahara, S. Hirose and J.D. Achenbach. Shape reconstruction of defects in an elastic solid. In *Symposium on Advances in NDT,* pp. 187-192. American Soc. Nondestructive Testing, 1996.

[32] K. Mayer, R. Marklein K.J. Langenberg and T. Kreutter. Three-dimensional imaging system based on Fourier transform synthetic aperture focusing technique. *Ultrasonics,* 28, July 1990.

[33] H.I. Schlaberg, M. Yang and B.S. Hoyle. Ultrasound reflection tomograpy for industrial processes. *Ultrasonics*, 36(1-5):297-303, Feb 1998.

[34] S.A. nielsen, J.T. Reinländer, K.K. Borum and H.E., Grundtoft. Tree-dimensional ultrasonic reflection tomography of cylindrical shaped specimens. In *7thECNDT*, p 2458-2465, May 1998.

[35] E.V. Malyrenko and M.K. Hinders. Fan beam and double crosshole lamb wave tomography for mapping flaws in aging aircraft structures. *Journal of the Acoustic Society of America*, 108(4):1631-1639, Oct 2000.

[36] I.D. Hall, A. MacNab and G. Hayward. Improved ultrasonic image generation through tomographic image fusion. *Ultrasonics*, 37(6):433-443, Sept 1999.

[37] V. Schmitz S. Chakhlov and W. Muller. Experiensces with synthetic aperture focusing technique in the field. *Ultrasonics,* pp. 731-738, 2000.

[38] M. Fink and J-F. Cardoso. Diffraction effects in pulse-echo measurements. *IEEE Transactions on Sonics and Ultrasonics,* SU-31(4), pp.313-329, July 1984.

[39] P. Wu and T. Stepinski. Inspection of copper canisters for spent nuclear fuel by means of ultrasonic array systems—modelling, defect detection and grain noise estimation. Technical report TR-99-12, Swedish Nuclear Fuel and Waste Management Co, 1998.

[40] K. Nagai. A new synthetic-aperture focusing method for ultrasonic B-scan imaging by Fourier transform. *IEEE Transactions on Sonics and Ultrasonics,* SU-32(4), pp. 531-536, July 1985.

[41] S.D. Silverstein and L.J. Thomas. Analytical comparison of sensor signal processing enhancements for NDT synthetic aperture ultrasonic imaging. *IEEE Transactions on Image Processing,* 2(1), January 1993.

[42] P. Wu and T. Stepinski. Spatial impulse response method for predicting pulse-echo fields from linear array with cylndrically concave surface. *IEEE Transactions on Ultrasonics, Ferroelectronics and Frequence Control,* 46(5), pp. 1283-1297, September 1999.

[43] P. Wu, F. Lingvall and T. Stepinski. Inspection of copper canisters for spent nuclear fuel by means of ultrasond—electron beam evaluation, harmonic imaging, materials characterisation and ultrasonic modeling. Technical report TR-00-23, Swedish Nuclear Fuel and Waste Management Co, 2000.

[44] A. Boström, UT-defect: A model for ultrasonic NDT of cracks. In *7th European Conference on NDT*, vol. 3, pp. 2414-2420, 1998.

2. THEORY FOR HARMONIC IMAGING OF WELDS

2. Theory for harmonic imaging of welds – Nonlinear wave theory

2.1 Introduction

In our recent report we presented results of an experimental study concerning harmonic imaging technology (HIT) in an attempt to apply the technology to ultrasonic NDE, in particular to the inspection of EB welds [1]. In that study we had exploited two types of harmonics for harmonic imaging (HI) of materials: (i) transducer harmonics that originate from the high order resonant modes of a transducer excited with a broad band signal, and (ii) material harmonics that result from the nonlinear propagation of ultrasound in materials. The techniques applying transducer and material harmonics to ultrasonic imaging of materials were called by us transducer HIT and material HIT, respectively [1]. In the present report, we will focus on the material harmonics and material HIT.

In the recent report we presented a systematical investigation of the material harmonic imaging. The experiments conducted using a copper block (Cu 2) with side-drilled holes as well as one canister specimen have shown the presence of harmonics generated in the copper material. We could detect the harmonics up to fourth order in the echoes from the side-drilled holes in the block Cu 2, also the harmonics up to third order were well pronounced in the scattering from the EB weld. The presence of harmonic generated by the copper material creates a potential application of harmonic imaging in NDE. Judging from the progress and success of the tissue HIT (some commercial medical ultrasound systems are already equipped with HIT) we may face a similar progress of the material HIT in the near future.

It is quite obvious that developing practical applications requires good theoretical models. With fast development of the tissue HIT, the nonlinear acoustic theories such as Burgers equation [2] and the KZK (Kuznetsov-Zabolotskaya-Khokhlov) equation [3, 4], that were established since 1940s have regained a great attention and have become the theoretical foundation of the tissue HIT. For example, an approach that is based on the spatial Fourier transform and the Burgers equation, proposed for calculating nonlinear diffractive acoustic fields [5] is used in the tissue HIT [6, 7]. Also a computer model for the tissue HIT that is based on the KZK equation has been developed very recently [8].

The material HIT initiated in our recent report has not been yet studied so extensively as the tissue HIT. The theories and computer models (for nonlinear elastic waves in solids) directly applicable to the material HIT have not yet been established, although material harmonics have been investigated in a limited scale and used to evaluate the nonlinear properties of materials [9, 10]. A rather comprehensive theoretical review of the nonlinear elastic waves in solids is given in [11], but the methods for implementing the nonlinear elastic wave theories (partial differential equations) presented there to material HIT are not established yet.

Our aim is to develop methods for implementing the existing nonlinear elastic theories and then to develop computer models for the material HIT. We are especially interested in a model for calculating

nonlinear elastic waves in immersed solids since the immersion inspection is used by us for copper canisters.

We are planning to establish the model for calculating nonlinear elastic waves in three steps: First, to model nonlinear propagation of plane waves in fluids, second, to investigate the reflection and refraction of nonlinear plane waves at the fluid/solid interface, and third, to build the model for nonlinear elastic waves in immersed solids. In the present work, we start with nonlinear propagation of plane waves in fluids. The method for studying the nonlinear plane waves is basically adopted from the existing literature [14-16] although some modification would be made to adapt it to our needs. In the future work we will continue the second and the third steps, so as to build a model used for the material HIT.

2.2   Concept of nonlinearity in nonlinear acoustics

What is the nonlinearity in the sense of nonlinear acoustics? To answer this question, let us first consider the definition of a linear system. A system H is linear if and only if

$$H[a_1 f_1(x) + a_2 f_2(x)] = a_1 H[f_1(x)] + a_2 H[f_2(x)], \tag{2.1}$$

for any arbitrary inputs $f_1(x)$ and $f_2(x)$, and any arbitrary constants a_1 and a_2. In other words, a linear system is the one that satisfies the superposition principle.
The simplest example is the linear algebraic equation as follows,

$$y = ax + b. \tag{2.2}$$

If

$$\frac{dy}{dx} = ax + b \tag{2.3}$$

and assuming thet $y=c$ when $x=0$, we have

$$y = \frac{1}{2} ax^2 + bx + c, \tag{2.4}$$

which is no longer linear (algebraic equation). As a matter of fact, we do call Eq. (2.3), or in general,

$$\frac{dy}{dx} = f(x) \tag{2.5}$$

a linear differential equation, even though the x dependence may not itself be linear.

Let us look at some more complicated cases. For example, the equation governing damped oscillations of spring/mass systems is

$$\frac{d^2 y}{dt^2} + 2\alpha \frac{dy}{dt} + \omega^2 y = 0, \tag{2.6}$$

where α and ω are constants; the Helmholz equation, the wave equation in the frequency domain, is

$$\nabla^2 p(\mathbf{r}, \omega) + \left(\frac{\omega}{c} + j\alpha(\omega) \right)^2 p(\mathbf{r}, \omega) = 0, \tag{2.7}$$

None of these equations (Eqs. (2.6) and (2.7)) are linear equations, but they are linear differential equations and describe linear systems and linear waves. It should be pointed that in Eq. (2.7) the attenuation $\alpha(\omega)$ can be nonlinearly related with frequency ω, but the equation still describes linear wave propagation.

Let us look at the Burgers equation of a frequently used form in nonlinear acoustics [13]

$$\frac{\partial p(z, \tau)}{\partial z} = \frac{\beta}{\rho_0 c_0^3} p \frac{\partial p}{\partial \tau} + \frac{\delta}{2 c_0^3} \frac{\partial^2 p}{\partial \tau^2}, \tag{2.8}$$

and the KZK equation [3, 4]

$$\frac{\partial^2 p(x, y, z, \tau)}{\partial z \partial \tau} = \frac{c_0}{2} \left(\frac{\partial^2 p}{\partial x^2} + \frac{\partial^2 p}{\partial y^2} \right) + \frac{\beta}{2 \rho_0 c_0^3} \frac{\partial^2 p^2}{\partial \tau^2} + \frac{\delta}{2 c_0^3} \frac{\partial^3 p}{\partial \tau^3}, \tag{2.9}$$

where $\tau = t - z/c_0$, and ω_0, c_0, β and δ are constant. The Burgers equation is a well-known equation that describes the nonlinear propagation of plane waves, and the KZK is an augmentation of the Burgers equation that describes nonlinear propagation of diffractive sound beams. The first term on the right hand side of the equality in Eq. (2.8), $p \partial p / \partial \tau$, and the second term in Eq. (2.9) $\partial^2 (p^2) / \partial \tau^2$ are the nonlinear. It is because of these nonlinear terms that the superposition principle of Eq. (2.1) does not hold for these equations. Thus both equations are nonlinear equations, and they describe nonlinear systems and nonlinear waves.

From the above analysis we may conclude that *the nonlinearities meant by nonlinear acoustics are phenomena of an acoustic nature that require a <u>nonlinear differential equation</u> for their description*.

Undertaking a study of nonlinear systems, one encounters the wide variety and diverse character of the phenomena. The vibrations of linear systems are all alike, but each nonlinear system is nonlinear in its own way. Therefore, every nonlinear problem is really individual. That is, it requires

individual, usually very complicated and difficult methods of analysis. The nonlinearity may occur in the source, in the medium, or even in the detection system.

2.3   Theory of nonlinear plane waves – Burgers equation and its solution

The Burgers equation is a very good approximation of the equations of motion for thermoviscous fluids when the wave motion is plane progressive [12]. To introduce the quantities used in the study, we look back to Eq. (2.8). In this equation, $\beta = 1 + B/2A$ is the coefficient of nonlinearity, $\tau = t - z/c_0$ the time retard, c_0 the small-signal sound speed, and δ the diffusivity of sound, which is given by

$$\delta = \frac{1}{\rho_0}\left(\frac{4}{3}\mu + \mu_B\right) + \frac{\kappa}{\rho_0}\left(\frac{1}{c_v} - \frac{1}{c_p}\right).$$
(2.10)

where, μ is shear viscocity, μ_B is bulk viscosity, κ is thermal conductivity, and c_v and c_p are the specific heats at constant volume and constant pressure, respectively. Thus, the Burgers equation accounts explicitly for the effects of nonlinearity (due to β) and thermoviscous dissipation (due to δ) on wave propagation. Note that the Burgers equation may have different forms [12, 2].

To apply Eq. (2.8) to depicting how a plane wave nonlinearly propagates, let us suppose that we have an infinite plane source at z=0 and the boundary condition on the source is given by

$$p(0,t) = P_0 f(t),$$
(2.11)

where P_0 is a pressure amplitude, and we find p as a function of t for $x \geq 0$. For a mono-frequency source with vibration frequency ω_0, the source condition is expressed as

$$P(0,t) = P_0 \sin(\omega_0 t),$$
(2.12)

and we are going to determine $P(x,t)$ for $x \geq 0$. In this mono-frequency case, the Burgers equation in Eq. (2.8) can be written as

$$\frac{\partial P}{\partial z} = \frac{\beta\,\omega_0}{\rho_0 c_0^3} P \frac{\partial P}{\partial \theta} + \frac{\delta\,\omega_0}{2c_0^3} \frac{\partial^2 P}{\partial \theta^2}.$$
(2.13)

where $\theta = \omega_0(t - z/c_0)$. Alternatively, the Burgers equation can be expressed in terms of particle velocity V as follows,

$$\frac{\partial V}{\partial z} = \frac{\beta\,\omega_0}{c_0^2} V \frac{\partial V}{\partial \vartheta} + \Gamma \frac{\partial^2 V}{\partial \theta^2},$$
(2.14)

where we have used the following relation,

$$\frac{P}{V} = \rho_0 c_0 ,$$ (2.15)

and $\Gamma = \delta \, \omega_0 / 2c_0^3$ is a constant related to the thermo-viscous dissipation of the medium, and consequently Γ is related to the energy loss in the medium. There are different methods for solving the Burgers equation for V or P, but one of the common methods is to use the Fourier series [14-16]. We use as a trial solution a Fourier series,

$$V(z) = \frac{1}{2} \sum_{n=-\infty}^{\infty} \widetilde{V}_n(z) \exp\left[jn(\omega_0 t - kz + \phi) \right].$$ (2.16)

where ϕ is an arbitrary phase constant and $\widetilde{V}_n(z)$ is the real amplitude of the nth harmonic. Using the relation $\theta = \omega_0 (t - z / c_0)$, the above equation can be rearranged in the following form,

$$V(z) = \frac{1}{2} \sum_{n=-\infty}^{\infty} V_n(z) \exp(jn\theta) .$$ (2.17)

where $V_n(z) = \widetilde{V}_n(z) \exp(jn\phi)$ is the complex amplitude. Obviously, $V_{-n}^*(z) = V_n(z)$ since $V_{-n}^*(z) = \left[\widetilde{V}_n(z) \exp(-jn\phi) \right]^* = \widetilde{V}_n(z) \exp(jn\phi) = V_n(z)$. Inserting Eq. (2.17) to Eq. (2.14), and after a lengthy manipulation (see Appendix 2A), we have

$$\frac{\partial V_n(z)}{\partial z} = \frac{j\beta \, \omega_0}{4c_0^2} n \left(\sum_{m=1}^{n-1} V_m(z) V_{n-m}(z) + 2 \sum_{m=n+1}^{\infty} V_m(z) V_{m-n}^*(z) \right) - \Gamma n^2 V_n(z), \; 0 < n < \infty$$ (2.18)

or alternatively,

$$\frac{\partial V_n(z)}{\partial z} = \frac{j\beta \, \omega_0}{2c_0^2} \left(\sum_{m=1}^{n-1} m V_m(z) V_{n-m}(z) + \sum_{m=n+1}^{\infty} n V_m(z) V_{m-n}^*(z) \right) - \Gamma n^2 V_n(z), \; \; 0 < n < \infty .$$ (2.19)

The first and second terms in the bracket in Eq. (2.18) or Eq. (2.19) represent, respectively, the accretion of the nth harmonic due to the preceding harmonics and the depletion due to higher harmonics, over the incremented distance.

An efficient method of solving Eq. (2.18) or (2.19) is a standard Runge-Kutta method that marches the solution forward over an incremental step Δz. Specifically, the incremental change of particle velocity $V(z, t)$ can be approximated by a truncated power series of the form

$$V(z + \Delta z) = V(z) + \frac{\partial V(z)}{\partial z} \Delta z ,$$ (2.20)

where quadratic and higher order terms are neglected. Substituting $\partial V / \partial z$ in Eq. (2.18) into (2.20), we have

$$V_n(z + \Delta z) = V_n(z) + \left\{ \frac{j\beta\,\omega_0}{4c_0^2} n \left[\sum_{m=1}^{n-1} V_m(z)V_{n-m}(z) + 2\sum_{m=n+1}^{\infty} V_m(z)V_{m-n}^*(z) \right] - \Gamma n^2 V_n(z) \right\} \Delta z , \quad (2.21)$$

which we will use for the computation. Only a finite number M of harmonics are retained in the computation. To facilitate the interpretation of how the fundamental and the harmonics of a plane wave change as the plane wave propagates, we write Eq. (2.21) in more detailed form. The fundamental is given by

$$V_1(z + \Delta z) = V_1(z) + \left[j\frac{\beta\omega_0}{4c_0^2} \left(\sum_{m=2}^{M} V_m(z)V^*_{m-1}(z) \right) - \alpha_0 V_1(z) \right] \Delta z , \quad (2.22)$$

which shows that the fundamental component is only subject to the depletion due to higher harmonics over the incremented distance. The higher harmonics are given by

$$V_2(z + \Delta z) = V_2(z) + \left[j\frac{\beta\omega_0}{4c_0^2} 2 \left(V_1(z)V_1(z) + 2\sum_{m=3}^{M} V_m(z)V^*_{m-2}(z) \right) - \alpha_0 2^b V_2(z) \right] \Delta z , \quad (2.23)$$

$$V_3(z + \Delta z) = V_3(z) + \left[j\frac{\beta\omega_0}{4c_0^2} 3 \left(\sum_{m=1}^{2} V_m(z)V_{3-m}(z) + 2\sum_{m=4}^{M} V_m(z)V^*_{m-3}(z) \right) - \alpha_0 3^b V_3(z) \right] \Delta z , \quad (2.24)$$

$$V_4(z + \Delta z) = V_4(z) + \left[j\frac{\beta\omega_0}{4c_0^2} 4 \left(\sum_{m=1}^{3} V_m(z)V_{4-m}(z) + 2\sum_{m=5}^{M} V_m(z)V^*_{m-4}(z) \right) - \alpha_0 4^b V_4(z) \right] \Delta z , \quad (2.25)$$

$$\cdots\cdots$$

$$V_n(z + \Delta z) = V_n(z) + \left[j\frac{\beta\omega_0}{4c_0^2} n \left(\sum_{m=1}^{n-1} V_m(z)V_{n-m}(z) + 2\sum_{m=n+1}^{M} V_m(z)V^*_{m-n}(z) \right) - \alpha_0 n^b V_n(z) \right] \Delta z . \quad (2.26)$$

Eqs. (2.23)–(2.26) show that the higher harmonics are subject to both the accretion due to the preceding harmonics and the depletion due to higher harmonics, over the incremented distance.

Assuming that $V_1(0)$ is known and that the maximum number of harmonics used is M, we can iteratively calculate $V_n(z + \Delta z)$ $(n = 2, ..., M)$ with step Δz.

2.4   Results and discussions

We have calculated nonlinear propagation of plane wave in terms of particle velocity Using Eq. (2.21). The program for the calculation is written in MATLAB. We assumed that the initial sinusoidal plane wave at z=0 has a frequency of $f = 5$MHz and an initial intensity of $I_0 = 10 \, \text{W/cm}^2$ that is equivalent to the initial particle velocity $V_1(0) = 0.0871$ m/s. The medium in which the wave propagates is water whose density and sound speed are $\rho_0 = 1000 \, \text{kg/m}^3$ and $c_0 = 1500 \, \text{m/s}$,

respectively, and it is assumed to be lossless, i.e., have no attenuation. The parameter B/A has a value of 5.2 for water at 30 °C [17]. The results shown in Fig 2.1 were calculated assuming the step $\Delta z = 0.2$ mm and 20 harmonics retained. From the figure we can see how the harmonics evolve as the wave propagates. The fundamental component decreases with the distance, which is because the fundamental depletes as the higher harmonics grow over the incremented distance. The higher harmonics increase with the distance, because the nth harmonic accretes as the lower harmonics deplete the over the incremented distance. On the whole, we may say that the nth harmonic builds up because it gains the energy from the lower harmonics.
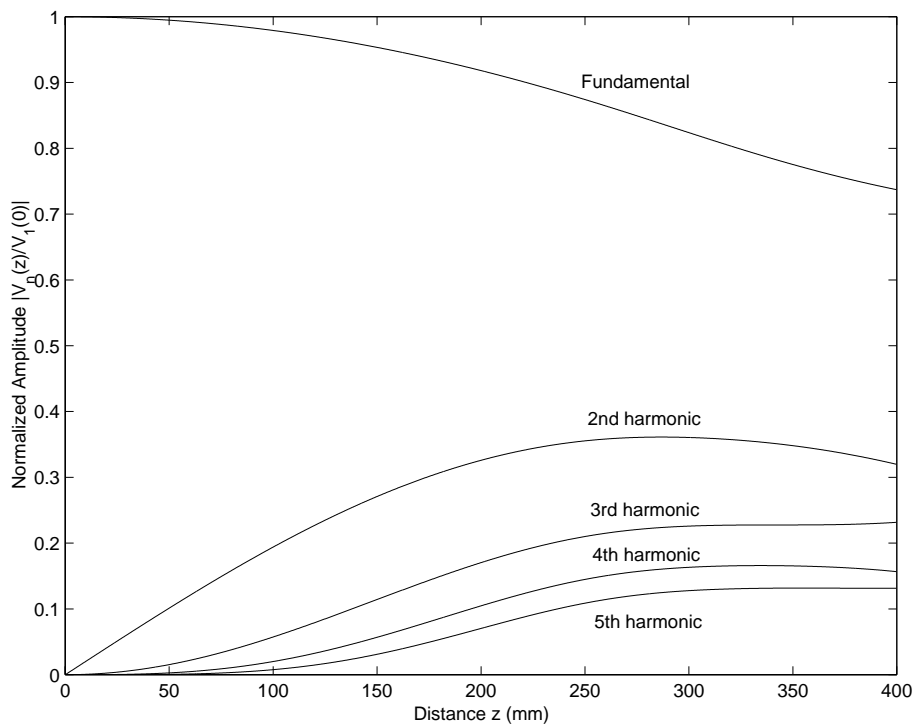

Fig. 2.1. Calculated harmonics in water due to an initial sinusoidal plane wave with frequency f =5MHz and initial intensity $I_0 = 10 \text{ W/cm}^2$ that is equivalent to $V_1(0)$ =0.0871 m/s.

2.5 Conclusion and future work

Nonlinear propagation of plane waves in fluids has been investigated based on the Burgers equation. The method for the study is basically adopted from the existing literature [14-16] although some modification has been made to adapt to our situation. The solution has been re-derived and two alternative forms feasible for computer calculation have been given. The Runge-Kutta method was used in the numerical calculation of the solution. The calculated results have shown how the harmonics evolve as the plane wave propagates.

It should be noted that the work presented here is just at its preliminary stage. We intend to use the presented model in our future work in which we plan to study nonlinear plane waves propagating

in layered media (because welds in copper canisters are always characterized by layered structures), including reflection and refraction at interface, and then to deal with more complicated cases, nonlinear propagation of ultrasonic beams in immersed solids (because welds in copper canisters may be inspected using ultrasonic beams in immersion case). As shown in the experimental study, using the material harmonic imaging technology one may catch a broader spectrum of information on inspected objects. The theoretical research may provide us with an useful guide to applying nonlinear waves so that the material harmonic imaging technology advances towards practical application, like the highly-developed tissue harmonic imaging in medical ultrasonic imaging. The goal of the present and future work is to build a simulation tool to model nonlinear elastic waves, which is a theoretical foundation of the material harmonic imaging technology.

2.6   References

[1]   P. Wu, Fredrik Lingvall, and T. Stepinski, *Inspection of Copper Canisters for Spent Nuclear Fuel by Means of Ultrasonic Array System – Electron Beam Evaluation, Materials Characterization* and *Modelling,* SKB Technical Report, 2000.

[2]   J. M. Burgers, "A mathematical model illustrating the theory of turbulence. In *Advances in Applied Mechanics*, Vol. 1, R. von Mises and T. von Kármán, eds. (Academic Press, New York), pp. 171-199, 1948.

[3]   E. A. Zabolotskaya, and R. V. Khokhlov, "Quasi-plane waves in the nonlinear acoustics of confined beams", *Sov. Phys. Acoust.* Vol. 15, pp. 35-40, 1969.

[4]   V. P. Kuznetsov, "Equations of nonlinear acoustics", *Sov. Phys. Acoust.* Vol. 16, pp. 467-470, 1971.

[5]   P. T. Christopher, and K. J. Parker, "New approaches to nonlinear diffractive field propagation", *J. Acoust. Soc. Am.* Vol. 90(1), pp. 488-499, 1991.

[6]   T. Christopher, "Finite amplitude distortion-based inhomogeneous pulse echo ultrasonic imaging," *IEEE Trans. Ultrason. Ferreoelect. Freq. Contr.*, Vol. 44, no. 1, pp. 125-139, 1997.

[7]   T. Christopher, "Experimental investigation of finite amplitude distortion-based, second harmonic pulse echo ultrasonic imaging," *IEEE Trans. Ultrason. Ferreoelect. Freq. Contr.*, Vol. 45, no. 1, pp. 158-162, 1998.

[8]   Y. Li, and J. A. Zagzebski, "Computer model for harmonic ultrasound imaging," *IEEE Trans. Ultrason. Ferreoelect. Freq. Contr.*, Vol. 47, no. 5, pp. 1259-1272, 2000.

[9]   M. A. Breazeale, "Ultrasonic studies of the nonlinear properties of solids," *Inter. J. Nondestr. Testing*, Vol. 4, pp. 149-166, 1972.

[10] M. A. Breazeale, and J. Philip, "Determination of their-order elastic constants from ultrasonic harmonic generation measurements," in *Physical Acoustics*, Vol. 17, edited by W. P. Mason, and R. N. Thurston, Academic Press: Orlando, Florida, pp. 1-60, 1984.

[11] A. N. Norris, "Finite-amplitude waves in solids," in *Nonlinear Acoustics*, edited by M. F. Hamilton, and D. T. Blackstock, Academic Press: San Diego, pp. 263-277, Chap. 9, 1998.

[12] D. T. Blackstock, "Thermoviscous attenuation of plane, periodic, finite amplitude sound waves", *J. Acoust. Soc. Am.* Vol. 36, pp. 534-542, 1964.

[13] M. F. Hamilton, and C. L. Morfey, "Model equations," in *Nonlinear Acoustics*, edited by M. F. Hamilton, and D. T. Blackstock, Academic Press: San Diego, pp. 41-63, Chap. 3, 1998.

[14] D. H. Trivett, and A. L. Van Buren, "Propagation of plane, cylindrical, and spherical finite amplitude waves", *J. Acoust. Soc. Am.* Vol. 69, no. 4, pp. 943-949, 1981.

[15] M. E. Haran, and B. D. Cook, "Distortion of finite amplitude ultrasound in lossy media", *J. Acoust. Soc. Am.* Vol. 73, no. 3, pp. 774-779, 1983.

[16] J. H. Ginsberg, and M. F. Hamilton "Computational methods," in *Nonlinear Acoustics*, edited by M. F. Hamilton, and D. T. Blackstock, Academic Press: San Diego, pp. 309-341, Chap. 9, 1998.

[17] R. T. Beyer, *Nonlinear Acoustics*. Naval Ship Systems Command: Washington D.C., Chap. 3, pp. 91-164, 1974.

Appendix 2A.

Inserting Eq. (2.17) to Eq. (2.14), we have

$$\frac{1}{2}\sum_{n=-\infty}^{\infty}\frac{\partial[V_n(z)\exp(jn\theta)]}{\partial z} = \frac{\beta\,\omega_0}{c_0^2}\left(\frac{1}{2}\sum_{n=-\infty}^{\infty}V_n(z)\exp(jn\theta)\right)\left(\frac{1}{2}\sum_{m=-\infty}^{\infty}\frac{\partial[V_n(z)\exp(jn\theta)]}{\partial\theta}\right)$$
$$+\Gamma\frac{1}{2}\sum_{n=-\infty}^{\infty}\frac{\partial^2[V_n(z)\exp(jn\theta)]}{\partial\theta^2}$$

(2A.1)

that is

$$\sum_{n=-\infty}^{\infty}\frac{\partial V_n(z)}{\partial z}\exp(jn\theta) = \frac{\beta\,\omega_0}{2c_0^2}\left(\sum_{n=-\infty}^{\infty}V_n(z)\exp(jn\theta)\right)\left(\sum_{n=-\infty}^{\infty}jnV_n(z)\exp(jn\theta)\right)$$
$$+\Gamma\sum_{n=-\infty}^{\infty}(-n^2)V_n(z)\exp(jn\theta)$$

(2A.2)

Noting that $\{V_m(z)\exp(jm\theta)\}\times\{(n-m)V_{n-m}(z)\exp[j(n-m)\theta]\} = V_m(z)(n-m)V_{n-m}(z)\exp(jn\theta)$, the above equation turns to be

$$\sum_{n=-\infty}^{\infty}\frac{\partial V_n(z)}{\partial z}\exp(jn\theta) = \frac{j\beta\,\omega_0}{2c_0^2}\sum_{n=-\infty}^{\infty}\left(\sum_{m=-\infty}^{\infty}(n-m)V_{n-m}(z)V_m(z)\right)\exp(jn\theta)$$
$$+\Gamma\sum_{n=-\infty}^{\infty}(-n^2)V_n(z)\exp(jn\theta)$$

(2A.3)

Comparing the terms on both sides of Eq. (2A.3), we obtain

$$\frac{\partial V_n(z)}{\partial z} = \frac{j\beta\,\omega_0}{2c_0^2}\sum_{m=-\infty}^{\infty}(n-m)V_{n-m}(z)V_m(z) - \Gamma n^2 V_n(z), \quad -\infty < n < \infty. \tag{2A.4}$$

Rearranging the first term on the right-hand side of Eq. (2A.4), we may have

$$\sum_{m=-\infty}^{\infty}(n-m)V_{n-m}(z)V_m(z) \overset{q=n-m}{=} \sum_{q=-\infty}^{\infty}qV_q(z)V_{n-q}(z) \overset{q=m}{=} \sum_{m=-\infty}^{\infty}mV_{n-m}(z)V_m(z). \quad -\infty < n < \infty. \tag{2A.5}$$

Substituting Eq. (2A.5) into Eq. (2A.4), Eq. (2A.4) becomes

$$\frac{\partial V_n(z)}{\partial z} = \frac{j\beta\,\omega_0}{2c_0^2}\sum_{m=-\infty}^{\infty}mV_{n-m}(z)V_m(z) - \Gamma n^2 V_n(z), \quad -\infty < n < \infty. \tag{2A.6}$$

Summing up Eqs. (2A.4) and (2A.6), we obtain

$$\frac{\partial V_n(z)}{\partial z} = \frac{j\beta\,\omega_0}{4c_0^2}n\sum_{m=-\infty}^{\infty}V_{n-m}(z)V_m(z) - \Gamma n^2 V_n(z), \quad -\infty < n < \infty. \tag{2A.7}$$

From Ginsberg and Hamilton [16], it follows that

$$\sum_{m=-\infty}^{\infty}V_{n-m}(z)V_m(z) = \sum_{m=1}^{n-1}V_m(z)V_{n-m}(z) + 2\sum_{m=n+1}^{\infty}V_m(z)V_{m-n}^*(z) \tag{2A.8}$$

where the relation $V_n(z) = V_{-n}^*(z)$ has been taken into account. In this way, the summation includes only quantities $V_n(z)$ for $n>0$. Thus, Eq. (2A.7) becomes,

$$\boxed{\frac{\partial V_n(z)}{\partial z} = \frac{j\beta\,\omega_0}{4c_0^2}n\left(\sum_{m=1}^{n-1}V_m(z)V_{n-m}(z) + 2\sum_{m=n+1}^{\infty}V_m(z)V_{m-n}^*(z)\right) - \Gamma n^2 V_n(z),} \quad 0 < n < \infty \tag{2A.9}$$

which is one of the final forms used in the computation. We can have an alternative form as follows

$$\frac{\partial V_n(z)}{\partial z} = \frac{j\beta \, \omega_0}{2c_0^2}\left(\sum_{m=1}^{n-1} mV_m(z)V_{n-m}(z) + \sum_{m=n+1}^{\infty} nV_m(z)V_{m-n}^*(z)\right) - \Gamma n^2 V_n(z), \quad 0 < n < \infty \quad (2A.10)$$

when we use the relation

$$\sum_{m=1}^{n-1} mV_m(z)V_{n-m}(z) = \frac{n}{2}\sum_{m=1}^{n-1} V_{n-m}(z)V_m(z) \tag{2A.11}$$

which can be simply results from the following derivation,

$$\sum_{m=1}^{n-1} mV_m(z)V_{n-m}(z) \stackrel{q=n-m}{=} \sum_{q=n-1}^{1}(n-q)V_{n-q}(z)V_q(z) \stackrel{q=m}{=} \sum_{m=n-1}^{1}(n-m)V_{n-m}(z)V_m(z)$$

$$= \sum_{m=1}^{n-1}(n-m)V_{n-m}(z)V_m(z) = \sum_{m=1}^{n-1} nV_{n-m}(z)V_m(z) - \sum_{m=1}^{n-1} mV_{n-m}(z)V_m(z)$$

$$\tag{2A.12}$$

3. ULTRASONIC IMAGING USING ACOUSTIC PHASE CONJUGATION 3-1

3. Ultrasonic Imaging using acoustic phase conjugation

3.1 Introduction

It is clear that reliable detection and characterization of defects in EB weld in copper requires high spatial and temporal resolution. Increased spatial resolution can be obtained by electronic beam focusing and post-processing ultrasonic data (synthetic focusing). Beam focusing and steering is performed by the hardware of Allin system. The array elements are excited individually in different time instants and the signals received by the array elements are delayed by analog delay lines. The resulting beam geometry is controlled by the applied focusing law, i.e., the delays used for the individual elements. The focusing law is found using geometrical optics for the inspection configuration defined by the respective sound velocities, array geometry, and sample geometry. The focusing law is established using some assumptions concerning, for instance, material homogeneity.

However, our previous research has shown that copper is inhomogeneous in the heat affected zone, and especially, in the weld zone [10]. This means that perfect focusing can never be obtained without detailed information about material structure, which obviously is unavailable before the inspection. Thus, compensation of the distortions must be self-adaptive since the designer has no a priori knowledge about them.

Similar problems have been encountered in astronomy when focusing telescopes located on the earth, as well as in medical ultrasound. The solution that was first developed in astronomy consists in using a technique referred to as *optical phase conjugation*. This technique has been also adapted to medical ultrasound where internal human organs are to be imaged using ultrasound beams penetrating inhomogeneous skin and fat layers. The technique used in ultrasound, depending on the means used for its realization, is known as *acoustic phase conjugation* or *time reversal mirrors*. Both methods make use of interesting features of phase conjugated waves, the difference is in the way of generating conjugated waves, acoustic phase conjugation uses frequency domain approach while the time reversal mirrors are realized in time domain .

A *phase conjugate wave* is defined as a wave that has the same spatial distribution as the incident wave but travels in the opposite direction. This phenomenon was first observed by Zel'dovich in a stimulated scattering of light [1]. After this discovery in 1972, phase conjugation has been extensively studied in optics [3], and this very interesting physical phenomenon has got a wide range of applications.

The purpose of this chapter is twofold: first, to introduce the concept of acoustical phase conjugation and review methods of its realization; second, to show how this technique can be applied to ultrasonic inspection of EB welds.

3.2 Conjugator theory (frequency approach)

In this section, we give an outline of the principle for generating acoustic phase conjugate waves. The basic explanation and the definition of phase conjugation and its characteristics are available, for example, in [1] and [4]. Here, we assume that we have a medium (called conjugator) in which the multiplication of an acoustic field and some other field (electric or electromagnetic) occurs. In other words, the conjugator enables a parametric interaction between both fields. Suppose an acoustic wave given by

$$u^i(\mathrm{r},t) = \tfrac{1}{2}U^i(\mathrm{r})\exp\{i(k^i\mathrm{r}-\omega t)\}+[\cdot]^* \qquad (1)$$

is incident on this medium. Here, k^i denotes the wave vector and $U^i(r)$ expresses the amplitude that is assumed to vary slowly compared to the wavelength. The complex conjugate is expressed by $[\cdot]^*$. Suppose the second field e^p, called the pump field, is given by

$$e^p(\mathrm{r},t) = \tfrac{1}{2}E^p\exp\{i(k^p\,\mathrm{r}-2\omega t)\}+[\cdot]^* \qquad (2)$$

is applied on this medium simultaneously (see Fig. 1). Its wave vector is denoted as k^p and the frequency is twice that of the incident acoustic wave. The amplitude E^p is assumed to be spatially uniform. Product of Eqs. (1) and (2) consists of four terms. The cross-term is expressed as

$$u^c(\mathrm{r},t) = \tfrac{1}{4}U^i(\mathrm{r})^* E^p \exp\{i[(k^p-k^i)\mathrm{r}-(2\omega-\omega)t]\}+[\cdot]^* \qquad (3)$$

This equation represents a wave with frequency is ω, the same as that of the incident acoustic wave, and with the amplitude proportional to $U^i(r)^*$. The wave vector of Eq. (3) is (k^p-k^i). Since the electromagnetic velocity c is about 10^5 times larger than any acoustic velocity v, the pump wave number $|k^p|=\dfrac{2\omega}{c}$ is negligible compared to the acoustic wave number $|k^i|=\dfrac{2\omega}{v}$. Therefore, Eq. (3) can be approximated as

$$u^c(\mathrm{r},t) = \tfrac{1}{4}U^i(\mathrm{r})^* E^p \exp\{i(-k^i\mathrm{r}-\omega t)\}+[\cdot]^* \qquad (4)$$

The field expressed by Eq. (4) has the same frequency as the incident acoustic wave and the spatial part $u^c(\mathrm{r},t) = \tfrac{1}{4}U^i(\mathrm{r})^* E^p \exp\{-ik^i\mathrm{r}\}$ is proportional to the complex conjugate of that of the incident wave. Therefore, this field is the *phase conjugate wave* of the incident acoustic wave.

Figure 1 shows the above-mentioned mechanism. The most notable feature of this method is that it does not need any kind of fine adjustments of geometry. In other words, the whole process is automatic.
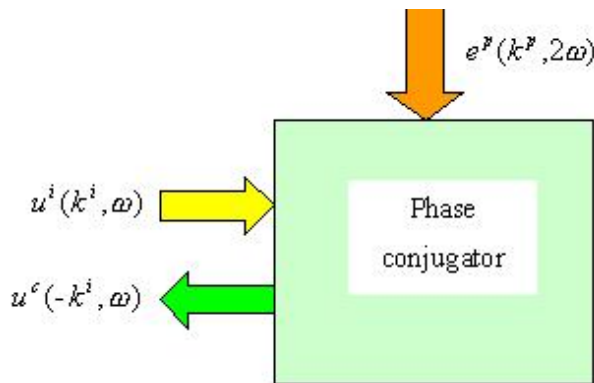

Fig. 1. Block structure of an acoustic conjugator.

The medium used for the conjugator must exhibit nonlinear characteristics to enable parametric interaction of the incident acoustic field and the pump field. There are two categories of materials used for this purpose, piezolectric and magnetic.

3.3 Review of conjugation methods

The methods for acoustic phase conjugation known today can be categorized into four groups: *purely acoustic method, nonlinear piezoelectric method, nonlinear magneto-acoustic method, and purely electrical method,* [1]. The first three methods involve some physical interaction between acoustic waves themselves or between acoustic waves and electromagnetic fields, whereas in the fourth method the effect is achieved using signal processing.

Most of the studies on the earliest stage belong to the first category of *purely acoustic methods*. Acoustic phase conjugate was generated experimentally via nonlinear effects in liquid containing bubbles, liquid surface, and thermal waves. Acoustic phase conjugate waves were also generated via four wave mixing (FWM) in liquid suspending small particles. These purely acoustic methods could be demonstrated at relatively low acoustic frequencies (kHz—MHz). This is because the nonlinear interaction occurs in liquid, in which the acoustic absorption is substantially large at higher frequencies.

The second category (*nonlinear piezoelectric method*) is based on the parametric interaction between acoustic waves at a frequency ω and an electric field at a frequency 2ω. The theory of this method is described above; nonlinear piezoelectric material is used as conjugator and electric field as pump field.

The third category (*nonlinear magneto-acoustic method*) which is also described by the above presented theory can be described as a magnetic counterpart of the piezoelectric method. Nonlinear magneto-acoustic media (e.g., α-Fe$_2$0$_3$ or hematites) are used as conjugator, and electomagnetic field

oscillating at frequency 2ω is used as pump field. An outstanding feature of this method is extremely high conversion ratio from the incident wave to the phase conjugate wave. The intensity of the phase conjugate wave is often larger than that of the incident wave, and sometimes larger by several 10 dB. Preobrazhensky *et al.* has reported on this method extensively [4] – [6]. It is very important for NDE applications that, in the two latter methods, operating acoustic frequency can be relatively high (MHz– GHz). This is related to the fact that these interactions occur in solid media, characterized by much smaller acoustic absorption than liquid.

The last category on our list *purely electrical methods,* often referred to as time reversal mirrors (TRM), have already found some practical applications. In these methods, no physical interaction is utilized, but instead, an array of ultrasonic transmitter/receiver elements, electrical circuits and signal processing algorithm perform the conjugation in time domain. The signals received from the inspected material by array elements are digitized and memorized. Then, the time-reversed waveforms are created and after amplification used for excitation of the same array elements. Although the fidelity of phase conjugate waves is not very high in this method, it has some advantages over other methods: the conversion ratio can be set arbitrarily, and the real-time or non-real-time operations are selectable. In these purely electrical methods, operating frequency is relatively low (kHz – MHz).

3.4   Application of time reversal to NDE

Fink *et. al.* [7, 8] has shown that time reversal mirror technique due to the invariance of the wave equation can be used to focus ultrasonic waves through heterogeneous lossless media. The invariance property means that, for each burst of sound that comes from a source and that can be refracted or scattered, there is a set of waves that precisely retrace all of the possible paths, ultimately converging at the original source. This property ensures that optimal focusing can be achieved by applying the time-reversal process on a closed surface covered with a 2D array of reversible transducers and surrounding the source.

Fink has introduced the concept of time-reversal cavity, where the divergent wave issued from a point-like source is sampled, time-reversed, and reemitted from the 2D array. Such a processing acts as an inverse filter of the diffraction transfer function that relates the wave-field propagation from the source to the closed surface.

In practice, since all arrays have limited aperture size a time-reversal cavity is difficult to realize and the time-reversal operator is only achieved over a limited area known as a time-reversal mirror (TRM). Its limited angular aperture results in a low-pass filter with relatively low cutoff frequency.

Despite the above limitations a number of applications have been demonstrated using the TRM technique. The technique was first aimed at a medical application of lithotripsy (breaking stones in kidneys)[8]. However, the maximum power of the available arrays has been insufficient for their

practical use. Some NDE applications have been also demonstrated, mainly for detecting hard-α particles in titanium material for aerospace engines, cf. [11].

The main disadvantages of the TRM technique seem to be its low fidelity and complexity of the required electronic hardware. The basic scheme of focusing on a point target through an inhomogeneous media requires three steps. In the first step (*illumination step*), the array illuminates an angular sector that contains the target. In the second step the echoes from the target, distorted by the inhomogeneous medium are recorded by the array (*receiving step*). Then in the last step (*focusing step*), the array retransmits the time-reversed field. When the target is spatially extended and/or when there are several targets in the illuminated beam, the time-reversal process needs to be iterated. The iterative mode allows selective focusing on the most reflective target and the final transmit beam converges on a small portion of this target. This means that a multi-channel hardware A/D converting the received signals, time-reversing and amplifying them is required for each array element. The fidelity is limited by the resolution of the A/D converters and the performance of the power amplifiers used in TRM system. To obtain a satisfactory time-reversal process, a high number of channels has to be used for the TRM aperture, which makes the hardware complex.

Therefore an alternative, less cumbersome method of self-focusing would be of great interest for the NDE applications. Recently, Ohno *et. al.* [1,2] have demonstrated the feasibility of the time reversal property and the automatic correction of phase distortion in phase conjugate process using nonlinear piezoceramics. They have demonstrated image improvement of a high contrast object placed in a special phase distorting jelly. Similar results were obtained for the magneto-elastic wave phase conjugator by Brysev *et. al.* [4, 5].

The advantages of nonlinear magneto-elastic method make it an interesting candidate in the competition with TRM and the piezoelectric method. Our direct contacts with one of the main developers of this method Prof. V. Preobrazhensky at EC-Lille have made realistic some preliminary experiments that will be presented below.

3.5   *Application of phase conjugation in magnetic ceramics to NDE*

One of the most promising methods of ultrasonic wave phase conjugation (WPC) is based on a strong parametric interaction of ultrasound waves with electromagnetic field in magneto-acoustic ceramics. A significant amplification of the phase conjugate wave is possible due the supercritical mode of parametric WPC, available in this type of materials [4, 5]. This valuable feature improves acoustic imaging by means of parametric phase conjugator in the case of high acoustical losses of the analyzed object. The gain obtained in the conjugator contributes to the increase of the overall signal to noise ratio of the imaging system.

A simplified scheme of the experimental conjugator setup used in the first experiments in conducted at EC-Lille in the laboratory of Prof. P. Pernod and Prof. V. Preobrazhensky, cf. [5], is shown in Fig. 2. An object was placed in the focal plane of a focalized ultrasonic transducer. Both object and transducer were immersed in a water tank. Symmetrically, on the other side of the object, a cylindrically shaped magneto-elastic phase conjugator (MPC) was introduced into the tank through a thin rubber membrane placed on the lateral side of the tank. The diameters of the transducer and the conjugator were 10 and 15 mm, respectively; the focal distance of the transducer was 30 mm. The conjugator had a length of 35 mm and was made of magneto-acoustic ceramics based on Ni-Co ferrite.
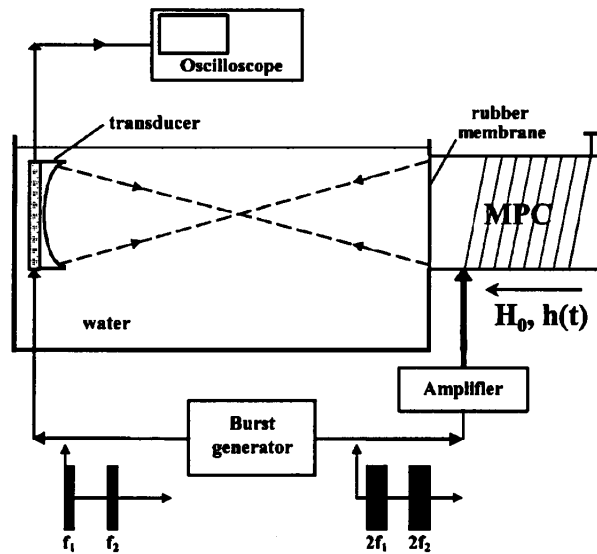

Fig. 2. MPC – magneto-acoustic phase conjugator. H_0 - externally produced dc magnetic bias field, applied to the coniugator; h(t) - alternating magnetic field of parametric pump (courtesy of Prof. Pernod).

The transducer was excited by a burst generator at a frequency of f =10 MHz with a duration of 2 µs. A sample consisting of an object and a special aberration layer was scanned line by line in the focal plane with a two-dimensional x-y positioning system. At the moment of arrival of the incident ultrasonic pulse in the active zone of the conjugator, the burst generator via an inductance coil applied an electromagnetic pumping field. The pumping burst duration was about 20 µs and its frequency was $2f$ = 20 MHz. The gain of the conjugator, measured in such conditions was 80 dB. A conjugate wave pulse, generated inside the conjugator propagated back to the source through the sample and was received by the transducer. During this propagation the processes of noise suppression and compensation of the discussed above phase distortions took place. A considerable improvement of images of small objects (electronic encapsulated integrated circuits) was demonstrated at frequency of 10 MHz.

Recently, we have made an attempt to investigate the feasibility of imaging of larger objects in the configuration presented in Figure 2. A small copper block with an EB weld was immersed in water between the transducer and the conjugator. It appeared, however, that the power of the transducer

operating at a relatively high frequency of 10 MHz was too low to conduct the experiments. Transducer with lower frequency (e.g., 5 MHz) has to be used for obtaining some results in this case. It appears, however, that despite the broadband character of the conjugation phenomenon (cf. [6]) lower transducer frequency requires substantial changes in hardware. First, the pumping coil and its amplifier are to be tuned to this frequency band. Second, the power of the transducer amplifier has to be increased and its operating frequency band also matched to the transducer. Therefore the experiment has been suspended until the required hardware modifications have been completed.

3.6 Concluding remarks

The theory of phase conjugation has been presented and different methods of wave phase conjugation (WPC) have been reviewed and characterized. Time domain method, known as time reversal mirrors has been reviewed in some detail with focus on its applications to NDT.

The ability of WPC to self-adaptive focus ultrasonic waves in inhomogeneous media makes it interesting in the application to the inspection of as EB welds.

The WPC can be performed in frequency-domain using nonlinear piezoelectric or magnetic materials. It can be also realized in time-domain using sophisticated, muli-channel array system.

The choice of magneto-acoustic phase conjugation, performed in nonlinear magnetic ceramics as a candidate for the feasibility demonstration has been motivated. Details of the preliminary experiment with high frequency NDE application (10 MHz), conducted at EC-Lille have been presented. The hardware used in this experiment has to be modified for lower operating frequency (approx. 5 MHz) to enable feasibility test on copper samples with EB weld. The experiments will be conducted in the near future in cooperation with Institut d'Electronique et de Microelecroélectronique du Nord (IEMN), Ecole Centrale de Lille.

3.7 References

[1]   M. Ohno, K. Yamamoto, A. Kokubo, K. Sakai, and K. Takagi, "Acoustic phase conjugation by nonlinear piezoelectricity". I. Principle and basic experiments. *J. Acoust. Soc. Am.*, **106**(3), September 1999, pp. 1330-1338.

[2]   K. Yamamoto, M. Ohno, A. Kokubo, K. Sakai, and K. Takagi, "Acoustic phase conjugation by nonlinear piezoelectricity. II. Visualization and application to imaging systems*", J. Acoust. Soc. Am.*, **106**(3), September 1999, pp. 1339-1345.

[3]   R.A. Fisher, Ed., *Optical Phase Conjugation*, academic Press, New York, 1983.

[4]   A.P. Brysev, L.M. Krutyanskii, V.L. Preobrazhenskii, "Wave phase conjugation of ultrasonic beams", *Physics.Uspekhi*, **41**(8), 1998, pp. 793-805.

[5]   A. Brysev, L. Krutyansky, P. Pernod, and V. Preobrazhenskii, "Acoustic microscope based on magneto-elastic wave phase conjugator", *Applied Phys. Letters*, **76**(21), May 2000, pp. 1-3.

[6]   L. Krutyansky, P. Pernod, and V. Preobrazhenskii, "Multi-frequency parameter phase conjugation of ultrasound beams in magnetic ceramics*", IEEE Trans. on Ultrason., Ferroelectr., and Frequency Control*, **UFFC-48(2)**, March 2001 2000, pp. 609-612.

[7]   M. Fink, "Time reversal of ultrasonic fields-Part I: Basic principles*", IEEE Trans. on Ultrason., Ferroelectr., and Frequency Control*, **UFFC-39(5)**, September 1992, pp. 555-566.

[8]   F. Wu, J-L. Thomas, and M. Fink, "Time reversal of ultrasonic fields-Part II: Experimental results", *IEEE Trans. on Ultrason., Ferroelectr., and Frequency Control*, **UFFC-39(5)**, September 1992, pp. 567-578.

[9]   M. Tanter, J-L. Thomas, and M. Fink, "Time reversal and the inverse filter*", J. Acoust. Soc. Am.*, **108**(1), July 2000, pp. 223-234.

[10] P. Wu, F. Lingvall, and T. Stepinski, "Inspection of copper canisters for spent nuclear fuel by means of Ultrasonic Array System, Electron beam evaluation, modelling and materials characterization", Technical Report TR-99-43, SKB, December, 1999.

[11] E. Kerbrat, C. Prada, D. Cassereau, R.K. Ing, and M. Fink, "Detection and imaging in complex media with the DORT method*", 2000 IEEE Ultrasonic Symposium,* Puerto Rico, October 22-25, 2000, pp.779-783.

4. Nondestructive characterization of cast iron

4.1 Introduction

Nondestructive characterization of steel aims at estimating material strengths, ductility, hardness or other mechanical parameters using the methods that do not impair material's functionality. The known NDE methods can measure the material properties only indirectly using mechanical vibrations, magnetic field or electromagnetic waves and radiation. The NDE parameters have to be correlated with the material properties experimentally and using complex theoretical models. In the case of cast iron most NDE methods are based on the analysis of its internal microstructure. Such parameters as contents and shape of graphite nodules or the structure of ferrite, austenite, pearlite colonies determine mechanical properties of cast iron.

Below, we present a short review of NDE methods used for the characterization of steels and cast iron.

4.1.1 Ultrasonic Waves

There are two mechanisms of interacting of ultrasonic waves with material microstructure, elastic and non-elastic. The *elastic interaction* takes the form of elastic waves that are subject to reflection, diffraction and scattering in the material. Velocity of the elastic waves is correlated with various material properties and is used as the main quantity that characterizes material microstructure.

The *non-elastic interaction* describes the dissipation of wave energy due to an absorption that contributes to material attenuation. The attenuation that is a sum of the absorption and scattering is also used for material characterization.

4.1.2 Resonant Ultrasonic Spectroscopy

Resonant Ultrasonic Spectroscopy (RUS) is a powerful tool for making accurate measurements of all the elastic modulus tensor elements and their imaginary counterparts, the internal friction or damping capacity [9]. It is a destructive technique in that it requires preparation of specimens with a regular geometry such as a sphere, cylinder or parallelepiped, but its results can be used to interpret any nondestructive measurement of an ultrasonic wave velocity or attenuation.

4.1.3 X-ray diffraction imaging

Electro-optical systems optimized for rapid x-ray diffraction imaging can be used to study crystal lattice rotation accompanying plastic deformation, to measure the rate of grain boundary migration during recrystallization annealing of cold-worked metals, to determine the physical state of exploding

metals, to monitor the amorphous to crystalline phase transformation of rapidly solidified metals, to rapidly measure residual stress (strain), and to study the dynamics of structural phase transitions.

4.1.4 Harmonic Analysis of Eddy Current Signals

Frequency domain evaluation of eddy current signals (harmonic analysis) in ferro-magnetic materials has been introduced in 90s as an industrial tool for materials characterization and proved to be a reliable and cost effective alternative to traditional techniques of quality control (metalography, mechanical tests, etc.) [3]. The harmonic analysis was applied to nodular cast iron samples characterization to predict their metallurgical and mechanical properties. The harmonic analysis of eddy current signals is performed using coil producing an electromagnetic field in the inspected material. This field is influenced by a secondary electromagnetic field (with opposite direction) that results from the induction of eddy currents inside of the material, and the magnetic behavior of the material. Changes of magnetic properties influence the signals in their amplitude and phase shifting.

For ferromagnetic materials the measured signal depends on the form of the hysteresis loop that in turn is dependent on the measuring frequency and the magnetic field intensity. The non-linearity of the hysteresis loop results in higher harmonic components that can be sensed using a separate pick-up coil. The mechanical and metallurgical parameters were found to have good correlation with the harmonic analysis parameters measured in the same samples, showing reliable industrial applicability of the technique. The main characteristics of the harmonic analysis system are the high measuring velocity and the high accuracy of measuring values that can be compared to destructive testing methods [3].

4.1.5 Measurement of Magnetostriction

In ferromagnetic materials particularly steel, the application of a magnetic field changes the dimensions of the sample. This phenomenon, called magnetostriction, can excite ultrasonic waves produced by the interaction of magnetic field with a coil of wire carrying an RF current at the frequency of the desired ultrasonic wave. The amplitude of the ultrasonic waves produced under these conditions can be used to measure the value of the magnetostrictive coefficients of the particular ferromagnetic material involved. In order to use such measurements as a nondestructive materials characterization tool, theoretical models relating the measured ultrasonic wave amplitudes to the magnetostriction coefficient have to be established.

From the above review we can select only two methods that are suitable for industrial applications: ultrasound and harmonic analysis of eddy current signals. However, the latter method has a serious drawback, due to the limited penetration of eddy currents (skin effect) it can be only used for the analysis near to the material surface. The most interesting, versatile and established seem to be the methods based on ultrasound. Elastic waves, like electromagnetic waves, are attenuated but a proper choice of frequency enables considerable penetration depths.

Table 1. Summary of methods used for nondestructive characterization of steels and cast iron.

Method	Physics	Used in industry?	Comments
Ultrasound	Elastic waves	yes	Sensitive to many parameters
RUS	Elastic waves	yes (for small components)	Requires well defined samples
X-ray diffraction	Electromagnetic waves	no	Sophisticated laboratory method
Harmonic analysis of EC	Magnetic	yes	Low penetration depth
Magnetostriction	Magnetic	no	Low penetration depth

Below, we will shortly present the principles of using ultrasound for characterizing cast iron.

4.2 Characterization of cast iron properties using ultrasound

In this section we will show how velocity, attenuation and scattering of elastic waves are correlated to the mechanical properties of cast iron. It should be noted however, that cast iron is an alloy of iron and carbon modified by minor additions of other elements, for instance, Si, Mn, P, Cr or Ni. Those elements result in a considerable variability of the iron's microstructure as well as its mechanical properties. Since the microstructure affects propagation of elastic waves in cast iron most works are concerned rather with the investigation of microstructure than direct estimation of its mechanical parameters.

Theory and experimental methods used for determining velocity, attenuation, and grain scattering in solids were established already in 70s in by E. P. Papadakis, who published his results in a series of papers ([13] can serve as an excellent review of his work). Important contributions have also been made by researchers from Stanford University, e.g. Grayeli and coworkers [5]. In Europe the Fraunhofer Inst. team led by K. Goebbels has also contributed to this field (see [4] for the review of their results). Recent works published in 90s report mainly practical results obtained for some specific types of cast irons [1, 2, 7].

4.2.1 Ultrasonic velocity

The relationship between the velocity of longitudinal, shear, and surface waves and the elastic modulus E, the Poison's ratio v and the material density ρ is well known. However, there are other factors that may influence the ultrasonic velocity that are less known [4]. Since the velocity depends on E and ρ several micro-structural effects can cause its change. A correlation between velocity and grain size and dislocation density has been proven experimentally. Residual and macroscopic stress, texture and scattering also influence the velocity.

Ultrasonic is relatively easy to measure, especially if relative measurements are sufficient for the application. The measurement requires samples with fairly flat and roughly parallel surfaces and can

be performed using a single transducer if the sample thickness is known accurately. However, in many industrial applications this can be difficult to achieve – sample thickness varying from sample to sample results in errors. A widely used industrial configuration, shown in Fig. 1 employing a water tank and two transducers eliminates this problem [6, 13]. The transducers are placed in water at the known distance L and the time of flight in water, t_0, is measured first (sound velocity in water depends on temperature). Then a metal sample with unknown thickness d is inserted between the transducers and the times t_1 and t_2 are measured.
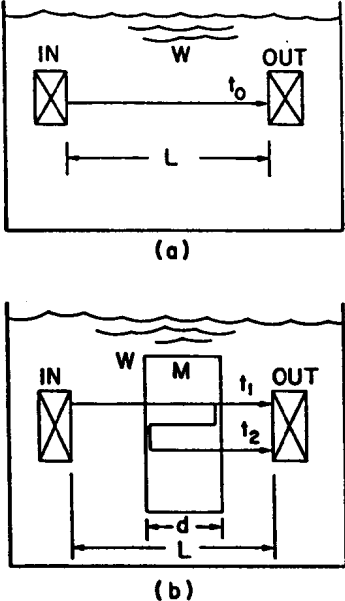

Fig. 1. Setup for measuring velocity in metal sample without knowledge of its thickness d. (a) Initial measurement in water. (b) Measurement of the times t_1 and t_2.

It can be shown that the sound velocity in metal, v_m is

$$v_m = \frac{(2t_0 - 3t_1 + t_2)}{t_2 - t_1} v_w; \qquad v_w = \frac{L}{t_0}$$

The absolute accurate measurement of velocity requires special techniques but accuracy of the above-presented method is sufficient for material characterization.

Pappadakis [13] reports results illustrating the relationship between the tensile and yield strength and ultrasonic velocity for nodular versus gray cast iron. Gray iron has a lower strength than the nodular iron due to the shape of carbon, which in the first case takes the form of flakes while in the second spheroidal particles or nodules. The carbon flakes in gray iron partially subdivide and weaken it relative to the nodular iron. The graphite flakes lower the elastic moduli in gray iron that is characterized by a lower ultrasonic velocity than the nodular iron. This is clearly pronounced in the results obtained by Ford Motor Company and presented by Pappadakis [13]. He reported that a 35%

increase in yield strength (or 55% increase in tensile strength) resulted in variations of the ultrasound velocity from 5330 m/s to 5700 m/s.

Similar results are also presented by Collins and Alcheikh [2], who investigated matrix structure and the graphite shape in cast iron. They reported variations of the ultrasound velocity from 4200 m/s for gray iron with graphite flakes, to 5600 m/s for the cast iron with 80 % nodularity.

4.2.2 Ultrasonic attenuation

The propagating ultrasonic wave is loosing its energy due to the absorption and scattering. Generally, attenuation coefficient is defined as a sum of the two respective terms, $\alpha = \alpha_A + \alpha_S$. Absorption results in converting part of the wave energy to heat. The following factors contribute to the absorption:

- Theromoelastic losses resulting from heating during compression, and cooling during dilatation.
- Dislocation damping that contributes strongly to the absorption in metals.
- Magnetoelastic losses in ferromagnetic materials.

All this effects are difficult to isolate and for the technical materials an absorption coefficient α_A is used that provides an indication of the total absorption observed for a given material.

Scattering occurs when the ultrasonic wave propagating in the inhomogenous material enters interfaces where the acoustic impedance ($Z = \rho v$) changes rapidly. This is observed for materials with distinct grain structure that is for all types of steel. The energy scattered at the grains is propagating in all directions resulting in energy loss in the main wave direction. Amount of scattering observed in a certain material depends on:

- The difference in the acoustic impedance ΔZ between the matrix and the grains,
- The ratio between the dimensions D of scatterers (grains) and the wavelength λ ,
- The volume density of the scatterers n_0

Scattering mechanisms have been studied in detail and it was shown that scattering by grains is responsible for a large part of the ultrasonic attenuation of polycrystalline metals [4, 11], and that scattering generally increases with frequency $\alpha_s = \alpha_s \left(f^n \right)$. Since scattering depends strongly on the ratio λ/D the following classification has been introduced to describe this mechanism [10]:

- $\lambda/D >> 1$ - Rayleigh scattering, signal amplitudes increase strongly with $\lambda/D \rightarrow \alpha_s \propto f^4$,
- $\lambda/D \sim 1$ - stochastic region, scattering ceases to increase $\rightarrow \alpha_s \propto f^2$
- $\lambda/D < 1$ – diffusion region, geometrical reflection $\rightarrow \alpha_s \propto f^0$.

It means that the amount of scattering for a given material depends strongly on frequency, especially in the Rayleigh region.

Measurement of scattering coefficient is rather complicated and requires more sophisticated methods than the measurement of velocity. First of all, a reliable coupling has to be established between the specimen and the transducer, for instance in immersion. Secondly, all losses due to transducer diffraction effects and the presence of transducer absorbing energy have to be compensated. Pappadakis invented a practical method employing a buffer rod between the transducer and the specimen (see Fig. 3) and also formulated practical rules for the diffraction correction for circular transducers, [12].
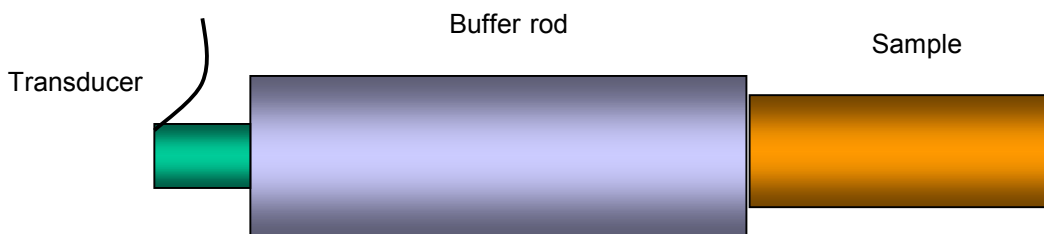

Fig. 3. A transducer and a specimen on a buffer rod

Thirdly, since attenuation is a function of frequency it has to be measured for the whole frequency spectrum of interest. Log-spectral difference and spectral difference method are used to establish the frequency dependence of attenuation coefficient, [8]. These methods have been described in a previous report [17] and here we will only present some results reported for steel and cast iron.

Pappadakis in his survey concerned with the attenuation measurement [15] quoted some results obtained for different steel structures that have been obtained by transformation of steel SAE 4150 by different cooling from the same austenitizing temperature. The attenuation for frequency 11 MHz changes from 0.011 dB/µs for tempered martensite to 1.0 dB/µs for perlite+ferrite. In his earlier work Pappadakis [14] investigated the attenuation in nodular cast iron and found that the attenuation curves for different types of cast iron in the frequency range 3 to 30 MHz were all of $\alpha \propto f^4$ type (Rayleigh scattering attenuation was dominating). Ahn and Lee [1] investigated attenuation as a function of carbon content in steel. Their conclusion was that the attenuation decreases as the carbon content increases because carbon reduces the average grain size (the measured attenuation was in the range 1 to 3 dB/µs for frequencies 6 to 10 MHz, respectively). Collins and Alcheikh reported their results from ultrasonic evaluation of cast steel, [2]. They found that the attenuation in cast iron decreases with increasing of its nodularity. They also ordered ductile iron matrix structures according to their attenuation for 2 and 4 MHz, the highest attenuation had tempered martensite and the lowest ferrite.

4.2.3 Ultrasonic backscattering

Although scattering can be measured indirectly by the measurement of ultrasonic attenuation, alternative methods have been developed for the measurement of backscattering, i.e., this portion of ultrasonic energy that comes back to the emitting transducer used in pulse-echo mode.

Since scattering depends strongly on the ratio λ/D it is a valuable source of information about material microstructure (grain dimensions). Theoretical models have been developed describing the relationship between the scatterers volume density, their dimensions and the amount of scattering observed [16]. Review of this works and the practical ways of measuring the backscattering can be found in our previous reports [17, 18], here we will limit ourselves to citing few references concerned with the application to cast iron.

To apply the abovementioned models to polycrystalline materials one has to assume that there is one dominating scatterer in the matrix. This assumption may be relevant for the nodular iron where graphite nodules are responsible for the scattering or for the pure iron that consists of ferrite grains. However, this assumption is not valid for heat-treated steels with more complex structure [1].

Kruger *et al* proposed a model for simulation of spectrum of the backscattered ultrasonic signal acquired from nodular cast iron [7]. Their preliminary results show a difference in the spectra obtained for the cast iron with different dimensions of nodules: 29 μm and 36 μm.

4.3 Conclusion

We have reviewed NDE methods suitable for the characterization of cast iron. Two groups of methods could be used in industrial environment, those based on ultrasound and on eddy current measurement. The latter group, however, has an inherent limitation – a low penetration depth, in practice less than a couple of millimeters. Therefore, our review has been focused on sensing the interaction of elastic waves with cast iron microstructure. We have explained how three different features of ultrasound, the sound velocity, the attenuation and the backscattering, can be used for the characterization. The two latter features are functions of frequency and contain a great deal of information about the material properties, especially its microstructure. Generally, an accurate measurement of velocity and particularly attenuation requires taking samples, while the backscattering does not. However, the extraction of the useful information concerning a particular type of cast iron from ultrasonic measurements is a complex issue that requires experimental work involving samples of this material.

4.4 References

[1] B. Ahn and S.S. Lee, "Effect of Microstructure of Low carbon Steels on Ultrasonic Attenuation", *IEEE Trans. Ultrasonics, Ferroacoustics and Frequency Control*, **UFFC 47:** 620-629, (2000).

[2] D.N. Collins and W. Alcheikh, "Ultrasonic non-destructive evaluation of the matrix structure and graphite shape in cast iron", *Journal of Materials Processing Technology*, **55:** 85-90, (1995).

[3] K.L. Feiste, M. Fetter, Ch. Reichert, W. Reimche ,and D. Stegeman, "Characterization of nodular Cast Iron Properties by Harmonic Analysis of Eddy Current Signals, in *Proc. of the ECNDT'98* (NDT.net, **3**, October 1998)

[4] K. Goebbels, S.Hirsenkorn, and H. Willems, "The Use of Ultrasound in the Determination of Microstructure: A Review", in *Proc. of the 1984 Ultrasonic Symposium*, pp. 841-846.

[5] N. Grayeli, D.B. Ilic, F. Stanke, C.H. Chou, and J.C. Shyne, "Studies of Steel Microstructure by Acoustical Methods", in *Proc. of the 1979 Ultrasonic Symposium*, pp. 273-277.

[6] J. Krautkrämer and H. Krautkrämer, *Ultrasonic Testing of Materials*. 4th Edition, Springer-Verlag, Berlin, (1990).

[7] S.E. Kruger, J.M.A. Rebello, and J. Charlier, "Ultrasonic Backscatteing Formulation Applied to Cast Iron Characterization", in *Proc. of the ECNDT'98* (NDT.net, **3**, November 1998)

[8] R. Kuc, "Estimation of acoustic attenuation from reflected ultrasound signals: Comparison of spectral-shift and spectral-difference approaches", *IEEE Trans. Acoust. Speech, Signals Process.* **ASSP-32:** 1-6 (1984).

[9] A.Migliori and J.L. Sarrao, *Ultrasound resonance Spectroscopy*, John Wiley and Sons, (1997).

[10] E.P. Papadakis, "Ultrasonic attenuation caused by scattering in polycrystalline media", *J. Acoust. Soc. Am.* **37:** 711-717 (1965).

[11] E.P. Papadakis, "Revised Grain-Scattering Formulas and Tables", *J. Acoust. Soc. Am.* **37:** 703-710 (1965).

[12] E.P. Papadakis, "Ultrasonic attenuation by spectrum analysis of pulses in buffer rods: Method and diffraction correction", *J. Acoust. Soc. Am.* **53:** 1336-1343 (1973).

[13] E.P. Papadakis, "Ultrasonic velocity and attenuation: measurement methods with scientific and industrial applications", in *Physical Acoustics*, ed. W.P. Mason, Academic Press, New York. **12**: 277-374 (1976).

[14] E.P. Papadakis, "Ultrasonic attenuation caused by Reileigh scattering by graphite nodules in nodular cast iron", *J. Acoust. Soc. Am.* **70:** 782-787 (1981).

[15] E.P. Papadakis, "The measurement of ultrasonic attenuation", in *Physical Acoustics*, ed. R.N. Thurston, and A.D. Pierce, Academic Press, San Diego. **19:**107-155 (1990).

[16] R.B. Thompson, F.J. Margetan, and Y.H.K. Han. "Relationship of microstructure to backscattered ultrasonic noise", in *Rev. of Progr. in Qantitative NDE*, vol. 11, pp. 1685-1691, 1992.

[17] P. Wu and T. Stepinski, "Inspection of copper canisters for spent nuclear fuel by means of Ultrasonic Array System, Modelling, defect detection and grain noise estimation", Technical Report TR-99-12, SKB, July, 1999.

[18] P. Wu, F. Lingvall, and T. Stepinski, "Inspection of copper canisters for spent nuclear fuel by means of Ultrasonic Array System, Electron beam evaluation, modelling and materials characterization", Technical Report TR-99-43, SKB, December, 1999.